

Selective clearance of the inner nuclear membrane protein emerin by vesicular transport during ER stress

Abigail Buchwalter^{1,2,3*}, Roberta Schulte⁴, Hsiao Tsai⁴, Juliana Capitano⁴, Martin Hetzer^{4*}

¹Cardiovascular Research Institute, University of California, San Francisco, San Francisco, United States; ²Department of Physiology, University of California, San Francisco, San Francisco, United States; ³Chan Zuckerberg Biohub, San Francisco, United States; ⁴The Salk Institute for Biological Studies, La Jolla, United States

Abstract The inner nuclear membrane (INM) is a subdomain of the endoplasmic reticulum (ER) that is gated by the nuclear pore complex. It is unknown whether proteins of the INM and ER are degraded through shared or distinct pathways in mammalian cells. We applied dynamic proteomics to profile protein half-lives and report that INM and ER residents turn over at similar rates, indicating that the INM's unique topology is not a barrier to turnover. Using a microscopy approach, we observed that the proteasome can degrade INM proteins in situ. However, we also uncovered evidence for selective, vesicular transport-mediated turnover of a single INM protein, emerin, that is potentiated by ER stress. Emerin is rapidly cleared from the INM by a mechanism that requires emerin's LEM domain to mediate vesicular trafficking to lysosomes. This work demonstrates that the INM can be dynamically remodeled in response to environmental inputs.

DOI: <https://doi.org/10.7554/eLife.49796.001>

***For correspondence:**

abigail.buchwalter@ucsf.edu (AB);
hetzer@salk.edu (MH)

Competing interests: The authors declare that no competing interests exist.

Funding: See page 26

Received: 29 June 2019

Accepted: 09 October 2019

Published: 10 October 2019

Reviewing editor: Elizabeth A Miller, MRC Laboratory of Molecular Biology, United Kingdom

© Copyright Buchwalter et al. This article is distributed under the terms of the [Creative Commons Attribution License](#), which permits unrestricted use and redistribution provided that the original author and source are credited.

Introduction

The biogenesis of roughly one-third of the cell's proteome takes place within the endoplasmic reticulum (ER) network. The ER is contiguous with the nuclear envelope (NE) membrane, a double bilayer membrane that defines the boundary of the nucleus. The NE is punctuated by nuclear pore complexes (NPCs) which control transport between the nuclear and cytoplasmic compartments. The outer nuclear membrane (ONM) and the bulk ER membrane network have a similar protein composition, including ribosomes that can be seen associated with the ONM. The inner nuclear membrane (INM), in contrast, is cloistered away from the bulk ER network by the NPC (**Figure 1A**). Proteomic analyses suggest that hundreds of proteins are selectively concentrated at the INM (**Schirmer et al., 2003**), and mutations to these proteins cause a broad array of rare pathologies (**Schreiber and Kennedy, 2013**).

As the INM is devoid of ribosomes and translocation machinery, INM proteins must be synthesized in the ONM/ER and transported into the INM. Proteins concentrate at the INM by mechanisms including diffusion followed by stable binding to a nuclear structure, such as chromatin or the nuclear lamina, or signal-mediated import through the NPC (**Katta et al., 2014**). Transport across the NPC is a major kinetic barrier to accumulation of proteins at the INM (**Boni et al., 2015; Ungricht et al., 2015**). While mechanisms of INM targeting have been extensively studied, it is less clear how INM proteins are targeted for degradation if misfolded, damaged, or mistargeted.

Protein folding is inefficient, and newly synthesized proteins often become terminally misfolded and require degradation (**Hegde and Zavodszky, 2019**). Mature proteins also become damaged or misfolded over time and require selective degradation and replacement. Within the ER membrane

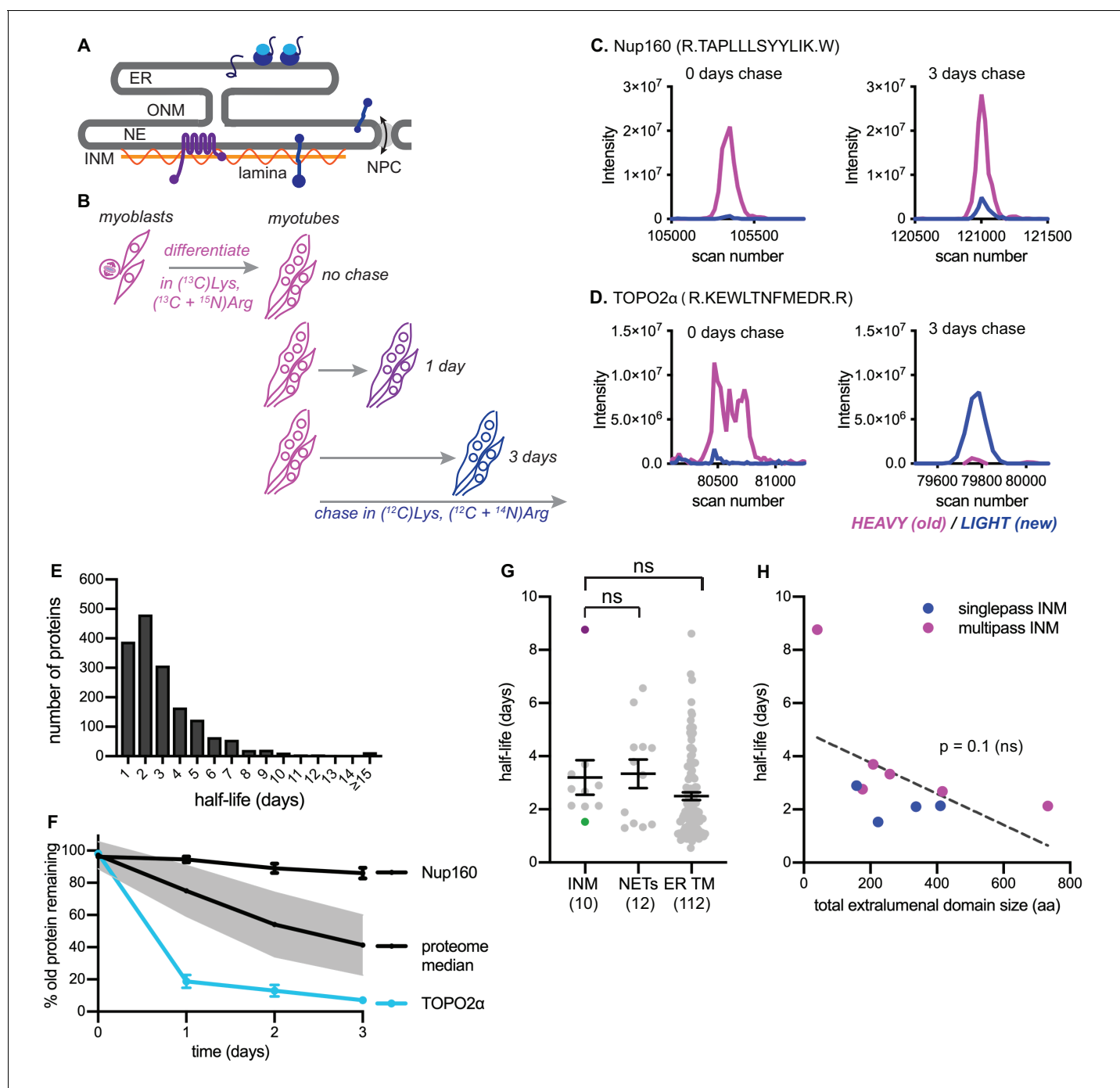


Figure 1. Dynamic proteomic analysis of inner nuclear membrane protein turnover. (A) Diagram of the ER with associated ribosomes, the NE composed of the ONM and INM, the NPCs, and the underlying nuclear lamina. INM proteins are synthesized in the ER, pass through the NPC, and enrich at the INM. (B) Overview of dynamic SILAC labeling experimental design. C2C12 mouse myoblasts were cultured for five population doublings in medium containing $^{13}\text{C}_6$ -lysine and $^{13}\text{C}_6$, $^{15}\text{N}_4$ -arginine to completely label the proteome. After 3 days of culturing under differentiating conditions to generate non-dividing myotubes, cultures were switched to chase medium containing ^{12}C -lysine and ^{12}C , ^{14}N -arginine for 1 to 3 days. Nuclear extracts were prepared at day 0, day 1, day 2, and day three for proteomic identification. (C,D) Representative peptide scans for a slowly degraded protein (Nup160) and (D) for a rapidly degraded protein (Topo2 α) at the starting and ending points of the experiment outlined in (B). (E) Histogram of calculated half-lives for 1677 proteins with a median half-life of 2.4 days. (F) Features of nuclear proteome turnover. Median turnover behavior of 1677 proteins detected in at least three timepoints with at least one peptide (black line) with one standard deviation (gray); compared to turnover of the slowly exchanged protein Nup160 (black) and the rapidly exchanged protein Topo2 α (blue). Error bars indicate SEM. (G) Calculated half-lives of 10 *bona fide* INM proteins, ranging from slowly degraded (nurim, purple) to rapidly degraded (emerin, green); 12 nuclear envelope transmembrane proteins (NETs) identified as NE residents by subtractive proteomics (see Schirmer et al., 2003); and 112 ER membrane proteins. ns indicates lack of

Figure 1 continued on next page

Figure 1 continued

statistical significance by Mann-Whitney test. Error bars indicate SEM. (H) There is no significant correlation between extraluminal domain size of INM proteins and their half-lives. See also Source Data 1–2, **Supplementary files 1–3**, and **Figure 1—figure supplement 1**.

DOI: <https://doi.org/10.7554/eLife.49796.002>

The following figure supplement is available for figure 1:

Figure supplement 1. Example half life fits.

DOI: <https://doi.org/10.7554/eLife.49796.003>

network, the major degradation pathway is ER-associated degradation, or ERAD. ERAD is initiated by poly-ubiquitination of a target protein by an E3 ubiquitin ligase, followed by extraction from the membrane and proteolysis by proteasomes in the cytosol (*Hegde and Zavodszky, 2019*). Flux through ERAD helps to maintain organelle homeostasis and cell function by clearing damaged, misfolded, or mislocalized proteins.

Recent work in *S. cerevisiae* has identified a small number of ubiquitin ligases that target INM-localized proteins for degradation by ERAD, but the mammalian homologs remain elusive, perhaps because of the massive expansion of the E3 ubiquitin ligase family in recent evolution (*Deshaies and Joazeiro, 2009*). Degradation of mammalian INM proteins also appears to rely on activity of the proteasome and on the ERAD ATPase p97 (*Tsai et al., 2016*), suggesting that mammalian INM proteins may be subject to ERAD. However, we lack a broad understanding of the lifetimes of INM proteins in this compartment and the pathways used for their degradation within mammalian cells.

We sought to understand features of INM protein turnover in mammalian cells, and applied both proteome-wide and targeted candidate approaches to address this question. Here we show that the LEM domain protein emerin (EMD) is a rapidly degraded constituent of the INM. We use EMD as a model for dissecting INM protein turnover pathways and demonstrate that EMD is subject to both proteasome-dependent and lysosome-dependent modes of degradation. We report that both misfolded and normally folded variants of EMD are selectively exported from the INM and ER during acute ER stress by vesicular transport through the secretory pathway and delivery to the lysosome. These findings indicate that the INM sub-compartment senses and responds to ER stress.

Results

Trends in protein turnover across the NE/ER membrane network

We first used a dynamic proteomic approach to understand trends in protein turnover across ER sub-compartments. Since the nucleus is entirely disassembled during mitosis in mammalian cells, we chose a system that would allow us to profile protein turnover in the absence of cell division. We made use of the C2C12 myoblast culture system, which can be induced to irreversibly differentiate into myotubes by serum withdrawal (*D'Angelo et al., 2009*). We subjected these non-dividing mouse muscle myotubes to a pulse-chase timecourse using stable isotope labeling in cell culture (SILAC) (*Ong and Mann, 2006*) for timepoints ranging from 1 to 3 days (**Figure 1B**, see Materials and methods). Crude nuclear extracts were prepared and analyzed by mass spectrometry, and the ratio of 'old' ($^{13}\text{C}_6\text{-Lys}$, $^{15}\text{N}_4$ + $^{13}\text{C}_6\text{-Arg}$ -labeled) to 'new' ($^{12}\text{C}_6\text{-Lys}$, $^{14}\text{N}_4$ + $^{12}\text{C}_6\text{-Arg}$ -labeled) protein was quantified at the peptide level over time; peptides that passed stringent quality control filters were retained for estimation of half-lives by a linear regression fitting method (*Dörrbaum et al., 2018*) (see Materials and methods). We evaluated 1677 proteins and predicted half-lives over a wide range, from less than a day to greater than 15 days (**Figure 1E**, Table S3). Linear regression performs well when a line can be fitted with high fidelity and a non-zero slope is detectable; these conditions were generally met for proteins with predicted half-lives ranging from 1 to 8 days. We observed more frequent deviations in linearity at the low extreme (predicted $t^{1/2} < 1$ day) and slopes approaching zero at the high extreme (predicted $t^{1/2} > 8$ days) (**Figure 1—figure supplement 1**). We expect that these factors limit the precision of half-life determination below 1 day and above 8 days from our 3 day timecourse. The median turnover rate that we observed (2.4 days) corresponds well with previous analyses in non-dividing mammalian cell cultures (*Cambridge et al., 2011*).

We observed some extremes in protein stability that are consistent with previous reports; for example, the long-lived nuclear pore complex component Nup160 (Toyama *et al.*, 2013) was in the top 10% of predicted half-lives, with a calculated half-life of approximately 18 days (Figure 1C,F, Table S1). Near the other extreme, we observed that the enzyme topoisomerase 2 α (Topo2 α) had a predicted half-life in the bottom 10%, of less than 1 day (Figure 1D,F). This is consistent with this enzyme's known regulation by ubiquitination and proteolysis (Gao *et al.*, 2014).

Having established this framework, we then quantified the turnover kinetics of known inner nuclear membrane (INM) proteins. For this analysis, we focused on proteins whose preferential enrichment in this membrane compartment had been experimentally verified; we identified ten such proteins in our dataset (see Table S1) and determined their half-lives (see Materials and methods). We observed half-lives for these proteins ranging from 8.8 days (nurim) to 1.5 days (emerin) (Figure 1G). While very little is known about nurim's function, its intrinsic biophysical properties may contribute to its long half-life: nurim contains six transmembrane domains, is extremely insoluble (Hofemeister and O'Hare, 2005), and diffuses very slowly within the INM (Rolls *et al.*, 1999). Emerin (EMD) is a founding member of the LEM domain family of INM proteins with essential functions in muscle development (Brachner and Foisner, 2011). Unlike nurim, EMD is a small (~25 kDa), single-pass, tail-anchored transmembrane protein that diffuses freely through the NPC and enriches at the INM by virtue of its affinity for lamin A (Vaughan *et al.*, 2001).

Given the INM's status as a restricted sub-compartment of the ER, we reasoned that it might be possible that INM proteins would be generally less accessible to protein turnover than ER membrane proteins. Alternatively, similarly effective turnover in both compartments might support the possibility that turnover can occur in situ at the INM. ER membrane proteins were well represented in our dataset, as a significant proportion of ER membranes remain attached to and co-purify with nuclei (Schirmer *et al.*, 2003). We could thus query whether INM proteins exhibited distinct turnover kinetics from membrane proteins of the bulk ER by comparing INM and ER transmembrane protein half-lives. We also compared *bona fide* INM proteins to proteins that had been identified as preferentially associated with either the inner or outer bilayer of the nuclear envelope (NE) membrane by comparative proteomics (Schirmer *et al.*, 2003), termed NE transmembrane proteins (NETs). Altogether, these analyses indicate that INM proteins do not exhibit unique turnover kinetics as a protein class, compared to ER membrane proteins in general or to the overlapping designation of NETs (Figure 1G).

The size of INM proteins determines whether a protein must rely on signal-mediated transport through the NPC (Katta *et al.*, 2014), and live imaging assays indicate that INM proteins with larger nucleoplasm-facing domains move more slowly across the NPC barrier (Boni *et al.*, 2015; Ungricht *et al.*, 2015). If transit across the NPC and out of the INM were a prerequisite for turnover in the bulk ER, we reasoned that turnover efficiency would also exhibit some dependence on protein size, because of the relationship between protein size and transport efficiency between the two compartments. The short half-life and small size of EMD is in line with this possibility. Our dataset of INM proteins included four single-pass INM and six multi-pass INM proteins, with total size of extraluminal domains ranging from 40 amino acids to 733 amino acids (Table S5). If export out of the NPC were a prerequisite for INM protein turnover, we reasoned that half-life should increase as the bulk of nucleoplasm-facing domains increases. We found no evidence for such a correlation (Figure 1H). We infer from this analysis that other factors distinct from monomeric protein size regulate protein turnover rate. This indicates that for INM proteins, export out of the INM is not a rate-limiting step for protein turnover. Rather, this is consistent with evidence in *S. cerevisiae* (Foresti *et al.*, 2013; Khmelinskii *et al.*, 2014) and in mammalian cells (Tsai *et al.*, 2016) that turnover of INM proteins can take place in situ at the INM.

Recombination-induced tag exchange confirms INM protein lifetimes

We observed a wide range of half-lives for INM proteins in our proteomic analyses (Figure 1G), with the polytopic INM protein nurim turning over most slowly and the single-pass INM protein EMD turning over most rapidly. To directly visualize these relative differences in protein stability, we used recombination-induced tag exchange (RITE) (Toyama *et al.*, 2019; Verzijlbergen *et al.*, 2010) (Figure 2A) to perform a microscopy-based pulse-chase experiment. We expressed either nurim or EMD in a cassette encoding two C-terminal epitope tags separated by LoxP sites and by a stop codon, such that the resulting transcript will encode a protein that will be C-terminally tagged with

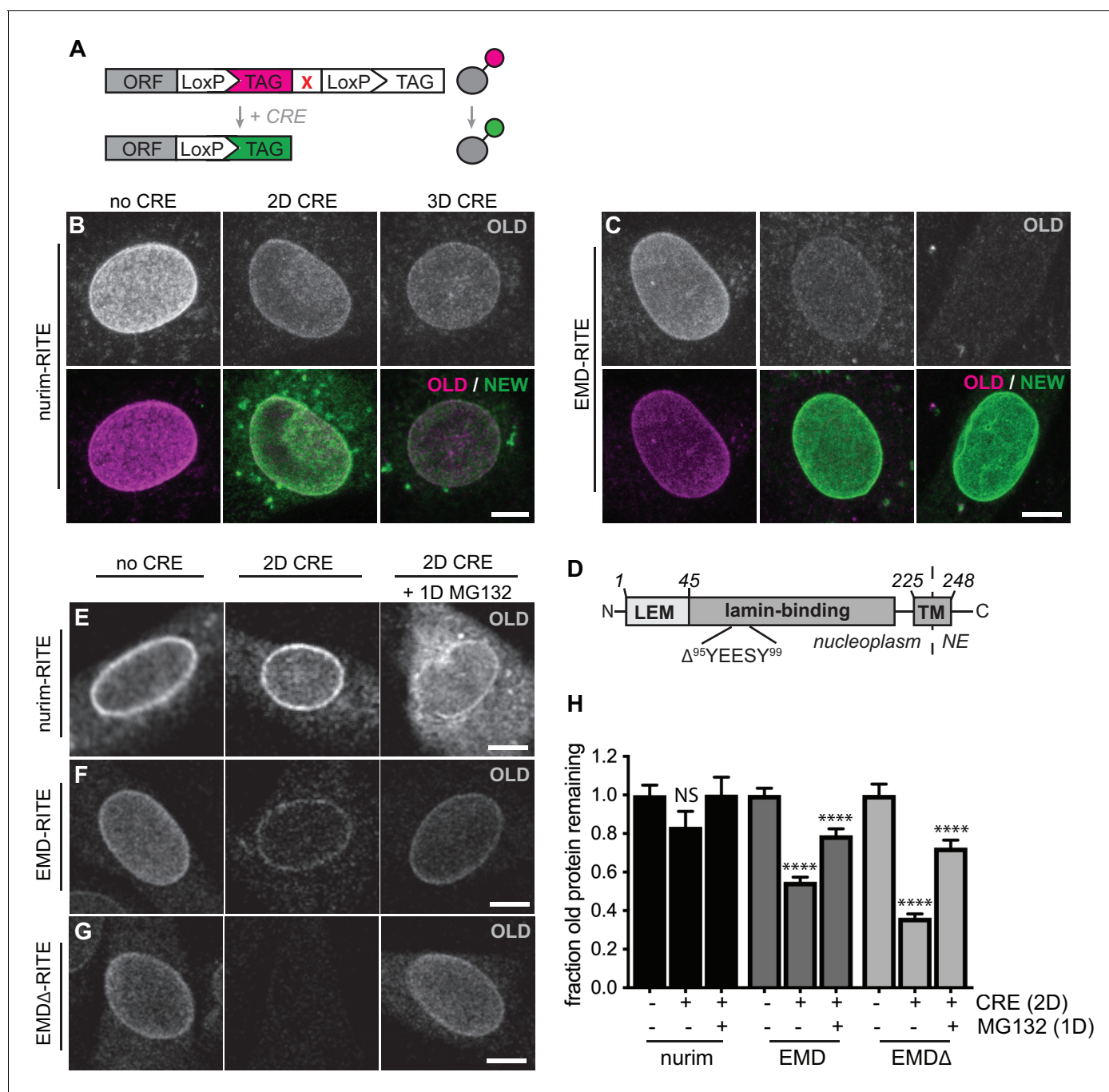


Figure 2. RITE analysis of INM proteins enables visualization of proteasome-dependent turnover. RITE analysis of INM proteins corroborates protein turnover determined by proteomics. (A) Schematic of recombination-induced tag exchange (RITE) expression cassette for visualizing protein turnover using Cre recombinase-mediated tag switching. (B-C) RITE timecourses of nurim-RITE (B) and EMD-RITE (C) in quiescent C2C12 cells. Maximum intensity projections of confocal z-series shown. (D) Diagram of emerin domain organization and position of EMD-linked deletion mutant (EMD Δ 95-99) within the lamin-binding domain. (E-G) RITE timecourses of nurim-RITE (E), EMD-RITE (F), and EMD Δ -RITE (G) with or without 1 day of cotreatment with the proteasome inhibitor MG132 (right panels). Single confocal z-slices shown. (H) Quantification of normalized intensity of old NE-localized RITE-tagged protein in maximum intensity projections of confocal z series acquired across the conditions shown in (E-G). Bars indicate average values with error bars indicating SEM for N > 42 cells per condition from 2 independent experiments. **** indicates p-value < 0.0001 (by t-test) for comparison between untreated and treated conditions. Scale bar, 10 μ m. See also **Figure 2—figure supplement 1**.

DOI: <https://doi.org/10.7554/eLife.49796.004>

The following figure supplement is available for figure 2:

Figure supplement 1. Identification of a disease-linked emerin mutant with normal NE localization.

Figure 2 continued on next page

Figure 2 continued

DOI: <https://doi.org/10.7554/eLife.49796.005>

the first tag. Upon adenoviral introduction of Cre recombinase, the RITE cassette is recombined to remove the first tag and position the second tag downstream of the open reading frame, so that all newly synthesized mRNA encodes a protein marked with the second tag. This enables simultaneous tracking of older and newer pools of protein that were synthesized before and after Cre addition, respectively (Toyama et al., 2019; Verzijlbergen et al., 2010). Using this approach, we visualized the rate of decline in the fluorescence intensity of 'old' myc-tagged nurim or EMD over several days in quiescent C2C12 cells. Consistent with our proteomic observations, we observed that RITE-tagged nurim decayed significantly more slowly than RITE-tagged EMD at the NE (Figure 2B–C,H).

The RITE system allows unambiguous dissection of the fates of maturely folded protein as well as nascent, newly synthesized protein. Recent work in yeast (Foresti et al., 2013; Khmelinskii et al., 2014) and in mammalian cells (Tsai et al., 2016) strongly suggests that INM proteins are subject to proteasome-mediated degradation via the ERAD pathway. The RITE system provides a means to distinguish the effects of proteasome inhibition on maturely folded proteins by inhibiting the proteasome after RITE tag switching, and monitoring the effects on maturely folded proteins. Mature nurim-RITE decreases only modestly within 2 days of tag switching, but co-incubation with the proteasome inhibitor MG132 for 1 day causes accumulation of nurim-RITE through the NE and ER (Figure 2E,H). Maturely folded EMD-RITE diminishes significantly at the NE within 2 days of tag switching but is partially stabilized at the NE in the presence of MG132 (Figure 2F,H). This indicates that mature, INM-localized proteins can be degraded in a proteasome-dependent pathway in situ at the INM. Notably, abundant proteasomes have been observed along the INM in cryo-EM studies and could possibly engage with substrate there (Albert et al., 2017). This is also consistent with a recent report that an unstable INM protein mutant accumulates within the nucleus of mammalian cells when the proteasome is inhibited (Tsai et al., 2016).

Identification of a model substrate for dissecting INM protein turnover

In order to gain more insight into the pathways that control INM protein turnover in mammalian cells, we chose to focus on EMD for its relatively fast turnover rate (Figure 1G, Table S1) and for the variety of disease-linked mutations to EMD that appear to influence protein stability (Fairley et al., 1999). Loss-of-function mutations to EMD cause Emery-Dreifuss muscular dystrophy (EDMD) (Bonne and Quijano-Roy, 2013). In some cases, EDMD-linked mutations cause loss of detectable EMD protein without affecting mRNA levels, suggesting that these mutations might cause misfolding and degradation of EMD (Fairley et al., 1999). We sought to identify such an EDMD-linked EMD variant for use as a model substrate for dissecting INM protein turnover. We selected a small in-frame deletion ($\Delta 95-99$) within EMD's lamin-binding domain (Figure 2D) that had been previously shown to localize to the NE when ectopically expressed (Fairley et al., 1999). Consistently, when we expressed either EMD-GFP or EMD $\Delta 95-99$ -GFP in C2C12 cells, we observed similar enrichment at the NE (Figure 2—figure supplement 1). Further, both protein variants exhibited identical residence times at the NE as assayed by fluorescence recovery after photobleaching (FRAP) analysis (Figure 2—figure supplement 1). Directly monitoring the stability of EMD $\Delta 95-99$ by RITE tagging indicates that it disappears from the NE faster than wild type EMD (Figure 2G), but is also stabilized at the NE by proteasome inhibition (Figure 2G–H). These observations indicate that EMD $\Delta 95-99$ is an unstable EMD variant that resides within the INM. We next moved to dissect that pathway(s) involved in EMD $\Delta 95-99$ degradation.

Proteasome-dependent and proteasome-independent modes of emerin clearance

Misfolded ER resident proteins are cleared by the ER-associated degradation (ERAD) pathway. ERAD clients are marked for degradation by ubiquitination, extracted from the ER membrane by the ATPase enzyme p97, and degraded by the proteasome in the cytosol (Ruggiano et al., 2014). INM proteins may also be targeted to an arm of the ERAD pathway in mammalian cells (Tsai et al., 2016), and our data indicate that multiple INM proteins are stabilized in situ by proteasome

inhibition. However, ubiquitin ligase(s) that recognize INM-localized substrates in mammalian cells have not been identified.

To sensitively probe factors that influence INM protein stability, we tracked the stability of GFP-tagged EMD variants. When de novo protein synthesis was blocked by cycloheximide (CHX), we observed rapid loss of EMD Δ 95–99-GFP within 4–8 hr (**Figure 3A–B**) while wild type EMD remained stable (**Figure 3—figure supplement 1**). This loss is blunted by co-treatment with the proteasome inhibitor MG132 (**Figure 3A**, third panel), consistent with our observations that INM protein turnover is slowed by proteasome inhibition using the RITE system (**Figure 2E–G**). If EMD Δ 95–99-GFP is directed to the proteasome through ERAD, inhibition of earlier steps in this pathway should similarly cause accumulation of EMD Δ 95–99-GFP. Indeed, pharmacological inhibition of p97 with the drug eeyarestatin I (**Wang et al., 2008**) causes modest accumulation of EMD Δ 95–99 and of higher molecular weight species, a similar effect to proteasome inhibition itself (**Figure 3B**). In contrast, the drug kifunensine, which prevents ERAD targeting of misfolded glycosylated proteins (**Fagioli and Sitia, 2001**), has no effect on EMD Δ 95–99-GFP levels as would be expected given the lack of glycosylation sites within EMD's small luminal domain (**Figure 3B**).

E3 ubiquitin ligases transfer ubiquitin to ERAD substrates, and each E3 ligase exhibits preference for a small number of substrates. A few E3 ligases have been implicated in ERAD of INM-localized substrates in yeast, including Doa10 and Asi1 (**Khmelinskii et al., 2014**). MARCH6 is a mammalian ortholog of Doa10 (**Zattas et al., 2016**). Mammalian orthologs of Asi1 have not been identified. Based on iterative sequence homology analysis through the MetaPhORs database (**Pryszcz et al., 2011**) we identified two possible Asi1 homologs: Rnf26 and CGRRF1. We depleted MARCH6, Rnf26, and CGRRF1 with short interfering RNA (siRNA), but observed no effect on EMD Δ 95–99 protein levels (**Figure 3—figure supplement 2**), suggesting that these ligases do not catalyze EMD turnover, or alternatively that multiple E3 ligases are redundant in this process. Importantly, the broad group of ERAD-implicated E3 ligases rely on a handful of E2 ubiquitin conjugating enzymes for ubiquitin transfer. These E2 ligases – four in mammals – thus represent a key control point for ERAD (**Christianson et al., 2011; Leto et al., 2019**). We targeted these four E2 ubiquitin ligases by siRNA transfection (**Figure 3—figure supplement 2**) and a subset of these by inducible RNAi using a potent microRNA-based system (**Fellmann et al., 2013**) and analyzed the effects on EMD Δ 95–99-GFP levels. To our surprise, knockdown of UBE2G1, UBE2G2, UBE2J1, and UBE2J2 either did not stabilize or instead decreased EMD Δ 95–99-GFP levels (**Figure 3C; Figure 3—figure supplement 2**). This finding suggests that when ERAD is perturbed, EMD variants can be cleared by an alternative pathway.

Emerin is subject to rapid stress-dependent clearance from the ER and NE

Global inhibition of ERAD places profound protein folding stress on the ER membrane network and induces the unfolded protein response (UPR) (**Christianson et al., 2011**). We considered whether direct induction of ER stress was sufficient to accelerate the turnover of EMD Δ 95–99-GFP. We tested the effect of the ER stressor thapsigargin (THG), which disrupts ER homeostasis by causing release of Ca²⁺ from the ER lumen, on EMD Δ 95–99 protein stability. Compared to CHX treatment alone (**Figure 3—figure supplement 1**), THG co-treatment further destabilized EMD Δ 95–99-GFP (**Figure 3D**). Strikingly, when we tracked EMD Δ 95–99 protein localization by time-lapse microscopy (**Figure 3E**), it became apparent that NE localization of EMD Δ 95–99 significantly decreases within 2 hr of THG treatment, concomitant with accumulation in a perinuclear membrane compartment that morphologically resembles the Golgi apparatus. By 8 hr after THG administration, EMD Δ 95–99 was undetectable (**Figure 3E–F**). These data suggest that under conditions of ER stress, EMD Δ 95–99 is cleared from the NE/ER membrane network by transport out of the ER and eventual disposal of the protein in a post-ER compartment.

Acute ER stress reroutes emerin through the secretory pathway

We took several approaches to test the possibility that EMD Δ 95–99 leaves the NE/ER network during ER stress. Firstly, we made use of the characteristic sugar modifications that occur as cargoes progress through the secretory pathway to determine whether EMD Δ 95–99 accesses post-ER compartments. Since the short luminal domain of EMD lacks a glycosylation consensus site, we

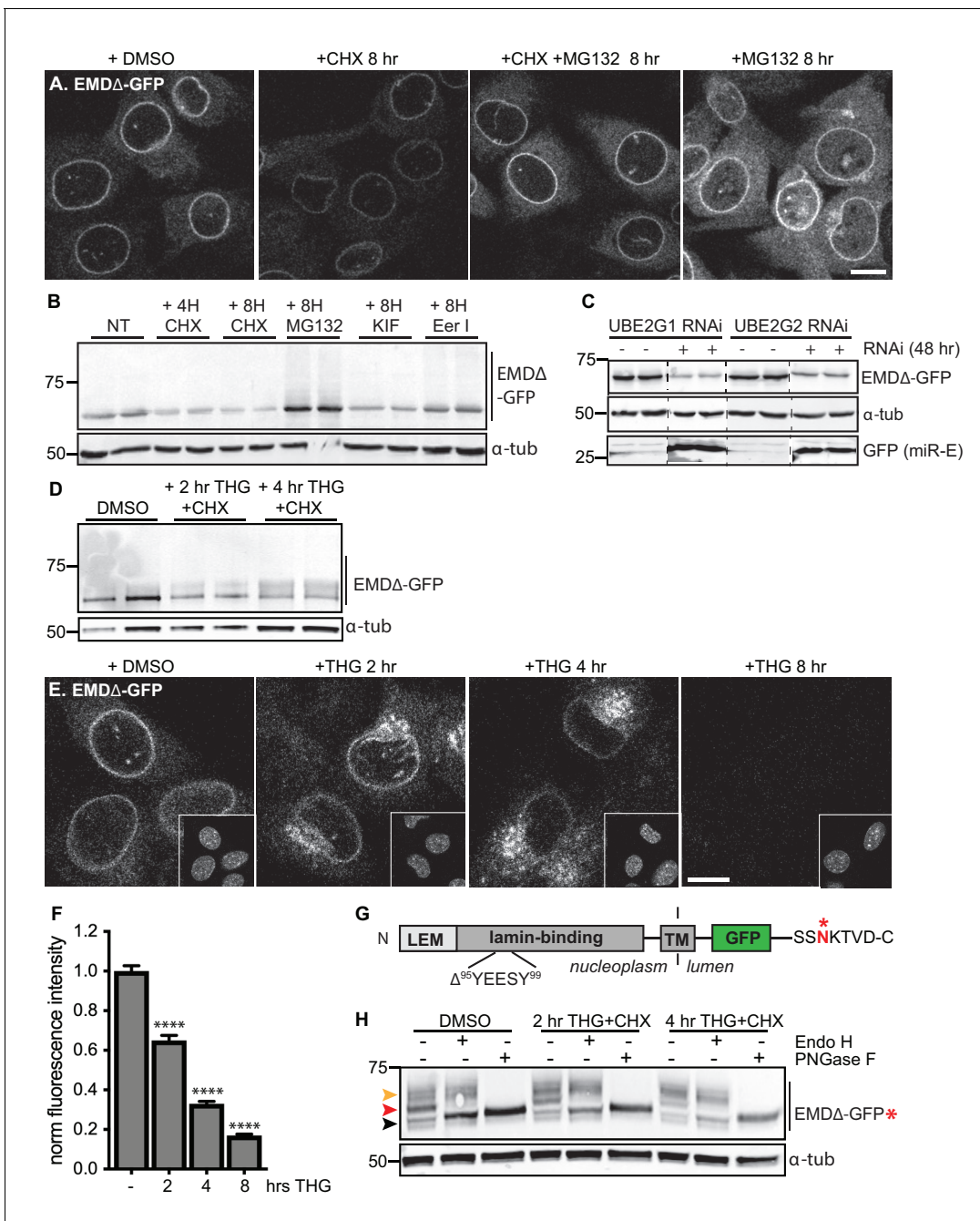


Figure 3. Acute stressors destabilize mutant emerlin protein levels. (A) C2C12 cells stably expressing EMDΔ-GFP and treated with DMSO vehicle control, CHX alone, CHX and MG132, or MG132 alone for 8 hours. All images were acquired using the same laser power and detector gain settings. Single confocal z slices shown. (B) Western blot analysis of protein levels in C2C12 cells stably expressing EMDΔ-GFP and treated with DMSO vehicle, the translation inhibitor CHX, the proteasome inhibitor MG132, the p97 ATPase inhibitor eeyarestatin, or the glycosylation trimming inhibitor kifunensine for the time periods shown. α-tubulin shown as loading control. (C) Western blot analysis of U2OS cells stably expressing EMDΔ-GFP and doxycycline-inducible RNAi targeting the E2 ubiquitin ligases UBE2G1 and UBE2G2 and treated with DMSO vehicle control (-) or with doxycycline (+) for 48 hours. Free GFP indicates RNAi induction. α-tubulin shown as loading control. (D) Western blot detection of EMDΔ-GFP levels in cells treated with DMSO vehicle, or co-treated with CHX and the ER stress inducer THG for the time periods shown. α-tubulin shown as loading control. (E) C2C12 cells stably expressing EMDΔ-GFP and treated with vehicle control or with THG for the time periods shown. Insets show nuclei in the same ~50 μm field of view stained with Hoechst. All images acquired using the same laser power and detector gain settings; single confocal z slices shown. (F) Quantification of total NE-localized GFP fluorescence in maximum intensity projections of confocal z slices acquired across the conditions shown in (E) for N > 410 cells per condition. (G) Diagram of emerlin domain organization and the sequence of an inserted C-terminal glycosylation sequence derived from the opsin protein, with glycosylation acceptor site marked (*). (H) Analysis of EMDΔ-GFP* glycosylation state in cells subjected to treatment with

Figure 3 continued on next page

Figure 3 continued

DMSO vehicle control or CHX and THG cotreatments for the times indicated. Red arrowhead indicates EndoH-sensitive glycosylated state of EMD Δ -GFP*; orange arrowhead indicates EndoH-resistant states of EMD Δ -GFP*; black arrowhead indicates deglycosylated EMD Δ -GFP*. α -tubulin shown as loading control. Numbers to left of blots indicate molecular weights in kDa. Scale bars in micrographs indicate 10 μ m. See also Figure 3 – figure supplement 1, 2, and 3.

DOI: <https://doi.org/10.7554/eLife.49796.006>

The following figure supplements are available for figure 3:

Figure supplement 1. Localization and stability of a disease-linked emerlin variant.

DOI: <https://doi.org/10.7554/eLife.49796.007>

Figure supplement 2. siRNA-mediated E2 or E3 ubiquitin ligase knockdowns do not stabilize EMD Δ -GFP.

DOI: <https://doi.org/10.7554/eLife.49796.008>

Figure supplement 3. Glycosylation reporter variants are destabilized by ER stress and recovered by BFA treatment.

DOI: <https://doi.org/10.7554/eLife.49796.009>

engineered the glycosylation site from the opsin protein (*Bulbarelli et al., 2002*) (SSNKTVD) onto the lumen-facing C terminus of EMD Δ 95–99. If EMD Δ 95–99 is retained in the ER, all of its N-linked glycans should remain sensitive to the trimming enzyme Endo H. On the other hand, if EMD Δ 95–99 exits the ER, its N-linked glycans will be elaborated with further modifications so that Endo H can no longer trim them. These glycosylation states can be detected as progressive increases in molecular weight, and can be completely removed by incubation with the enzyme PNGase F. This engineered variant, EMD Δ 95–99-GFP*, localizes normally to the NE and also disappears from the NE upon ER stress induction (**Figure 3—figure supplement 3**). In unstressed cells, EMD Δ 95–99-GFP* is predominantly observed in an Endo H-sensitive glycosylation state (**Figure 3H**, red arrowhead), with a minor pool of Endo H-resistant protein (**Figure 3H**, orange arrowhead). In contrast, EMD Δ 95–99-GFP* shifts progressively to a higher molecular weight, Endo H-resistant state over 2 to 4 hr of co-treatment with CHX and THG. This indicates that ER stress induction increases the proportion of EMD Δ 95–99 that exits the NE/ER and samples post-ER compartments.

Upon ER stress induction, EMD Δ 95–99-GFP accumulates in a perinuclear domain that resembles the Golgi apparatus (**Figure 3E**). We evaluated the extent of colocalization of EMD Δ 95–99-GFP with the medial Golgi resident protein giantin in untreated cells and cells that had been treated with THG for 2–4 hr (**Figure 4A–C**). In untreated cells, EMD Δ 95–99-GFP was not detectable in the Golgi, but THG treatment rapidly induced Golgi colocalization as NE-localized EMD Δ 95–99 levels decreased (**Figure 4A–C**). Comparing GFP fluorescence intensity in the Golgi versus the NE over time revealed that ER stress induces significant enrichment of EMD Δ 95–99-GFP in the Golgi accompanied by loss from the NE within 2 hr (**Figure 4D**).

EMD Δ 95–99 could be delivered to the Golgi by vesicular transport from the ER. Transport between the ER and the Golgi is mediated by packaging of cargoes into COP-coated vesicles (*Barlowe and Miller, 2013*), a process which can be inhibited by the drug brefeldin A (BFA). BFA acts by disrupting COPI vesicle formation, leading to the collapse of the Golgi into the ER membrane network (*Chardin and McCormick, 1999*). To test whether clearance of EMD Δ 95–99-GFP from the NE/ER requires vesicle-mediated ER-to-Golgi transport, we co-incubated cells expressing EMD Δ 95–99-GFP with THG and BFA. Strikingly, co-treatment with BFA nearly quantitatively reversed loss of EMD Δ 95–99-GFP from the NE (**Figure 4E–F**). Taken together with the time-dependent enrichment of EMD variants in the Golgi apparatus (**Figure 4A–C**), and the time-dependent accumulation of more complex N-glycosylated variants of EMD Δ 95–99-GFP* (**Figure 3H**), this indicates that under ER stress, EMD variants can be cleared from both the NE and ER by vesicular transport through the Golgi.

While vesicle-mediated transport is the major pathway by which proteins move from the ER and onward through the secretory pathway, alternative modes of removing protein from the ER exist, in particular during ER stress. Recent evidence indicates that the ER can undergo autophagy under various conditions, including acute ER stress (*Smith et al., 2018*). To evaluate the possibility that EMD Δ 95–99-GFP could be engulfed and removed from the NE and ER by autophagosomes, we tested the ability of the PI3K inhibitor KU55933 to reverse EMD Δ 95–99-GFP loss. PI3K signaling promotes the formation of isolation membranes that engulf autophagic cargo (*Farkas et al., 2011; Klionsky et al., 2016*). We observed that cotreatment with KU55933 during acute ER stress could

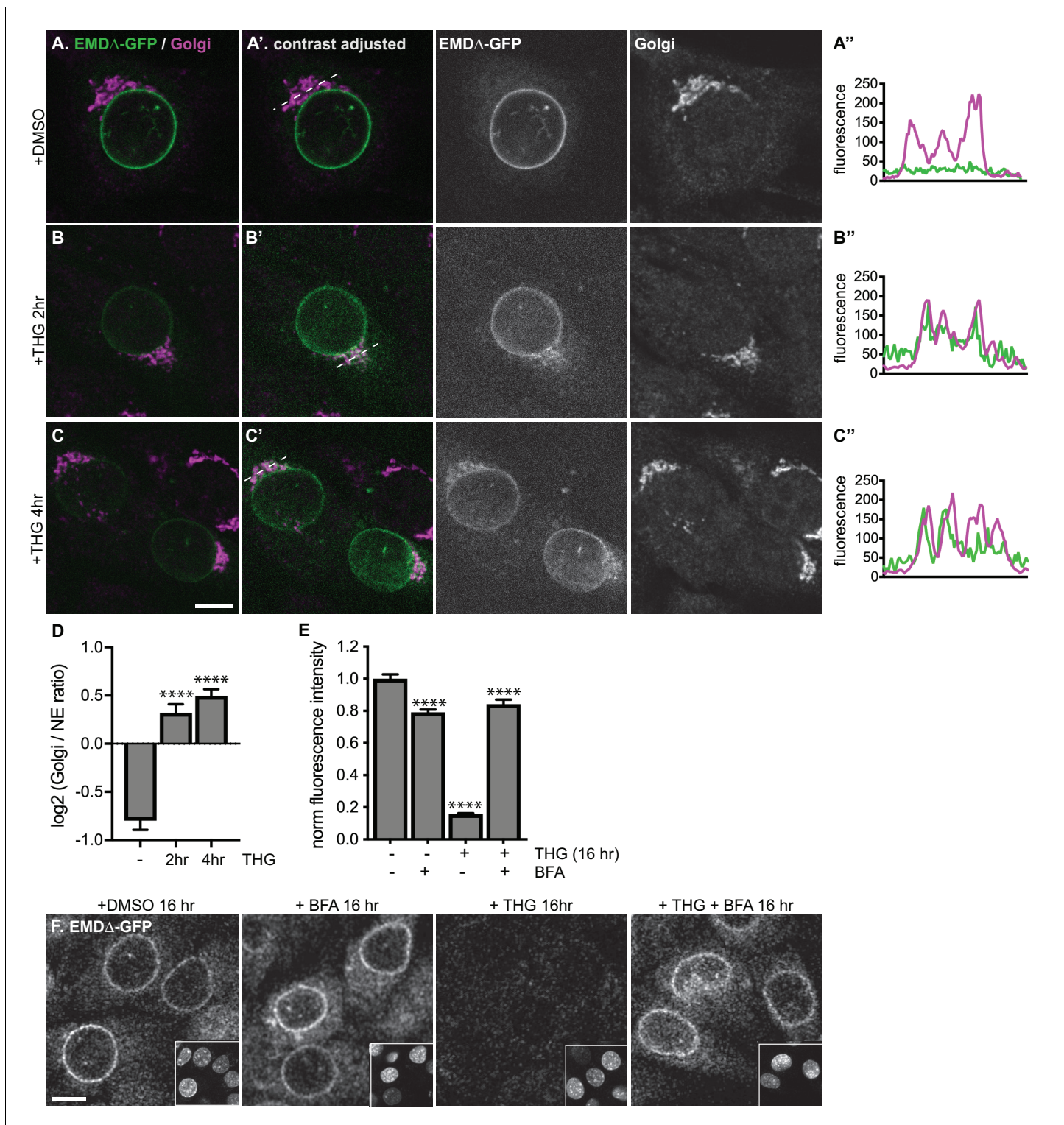


Figure 4. Stress-induced clearance of mutant emerin from the ER and NE involves the secretory pathway. (A-C) Representative confocal slices of cells stably expressing EMD Δ -GFP, treated with DMSO or THG for the indicated times and costained for giantin to mark the Golgi (magenta). All images were acquired using the same laser power and detector gain settings. (A'-C') Are contrast-adjusted to show relative levels of EMD Δ -GFP in NE and Golgi. Dotted lines mark positions of linescans in (A''-C''). (D) Quantification of GFP fluorescence intensity abundance ratio in Golgi versus NE in single, non-contrast-adjusted z slices over THG treatment timecourse. Columns indicate average with error bars indicating SEM for N > 37 cells from two independent experiments. **** indicates p-value < 0.0001 compared to untreated (by t-test). (E-F) Representative confocal slices of cells stably expressing EMD Δ -GFP (F) after 16 hr of treatment with DMSO vehicle control, THG, BFA, or co-treatment with THG and BFA. All images were acquired

Figure 4 continued on next page

Figure 4 continued

using the same laser power and detector gain settings. Insets show nuclei in the same $\sim 50 \mu\text{m}$ field of view stained with Hoechst. (E) Quantification of GFP fluorescence intensity at the NE in maximum intensity projections of confocal z series acquired across the conditions represented in (F). Columns indicate average with error bars indicating SEM for $N > 386$ cells from three independent experiments. **** indicates $p\text{-value} < 0.0001$ compared to untreated (by t-test). Scale bars in micrographs indicate $10 \mu\text{m}$. See also **Figure 4—figure supplement 1**.

DOI: <https://doi.org/10.7554/eLife.49796.010>

The following figure supplement is available for figure 4:

Figure supplement 1. Colocalization of emerin with the Golgi.

DOI: <https://doi.org/10.7554/eLife.49796.011>

not prevent loss of EMD $\Delta 95$ –99-GFP from the NE/ER (**Figure 5A–C**), in contrast to the ability of BFA treatment to rescue EMD loss. This indicates that vesicle-mediated transport to the Golgi and not autophagic engulfment mediates EMD $\Delta 95$ –99-GFP's exit from the ER during stress.

Proteins in post-ER compartments can be degraded by vesicle-mediated traffic to the lysosome (**Saftig and Klumperman, 2009**). To investigate whether the lysosome was the eventual destination of EMD $\Delta 95$ –99-GFP after ER export, we co-incubated cells expressing EMD $\Delta 95$ –99-GFP with THG and bafilomycin A1 (Baf A1), which impairs lysosome acidification and thus slows protein degradative processes within lysosomes.

Under these conditions, we observed complete translocation of EMD $\Delta 95$ –99-GFP out of the NE and ER and into numerous vesicles that are decorated with the lysosomal marker LAMP1 (**Figure 5F**). Notably, bafilomycin A1 alone did not trap EMD $\Delta 95$ –99-GFP in lysosomes (**Figure 5E**), indicating that ER stress potentiates exit from the NE/ER and lysosomal accumulation. This indicates that the eventual destination of EMD $\Delta 95$ –99-GFP after export from the NE/ER network is the lysosome.

If EMD $\Delta 95$ –99 arrives at the lysosome by trafficking through the secretory pathway, this should be accompanied by the accumulation of Endo H-resistant N-glycosylation modifications on our engineered reporter EMD $\Delta 95$ –99-GFP*. Indeed, we observe that the majority of EMD $\Delta 95$ –99-GFP* exists as an Endo H-sensitive species in unperturbed cells (**Figure 5G**, red arrowhead), but shifts progressively to a higher molecular weight, Endo H-resistant state over 2 to 4 hr of co-treatment with THG and Baf A1 (**Figure 5G**, orange arrowhead). This indicates that EMD $\Delta 95$ –99 traverses the secretory pathway before being delivered to the lysosome.

Emerin transiently accesses the plasma membrane during ER stress

A possible route from the early secretory pathway to the lysosome could involve anterograde transport following the 'bulk flow' of the secretory pathway, through the Golgi and into vesicles destined for the plasma membrane (PM). There, mislocalized proteins may be selectively endocytosed and trafficked to lysosomes for degradation through retrograde transport (**Saftig and Klumperman, 2009**). To explore this possibility, we performed antibody uptake assays in cells expressing EMD $\Delta 95$ –99-GFP under homeostatic or stressed conditions. EMD is a tail-anchored protein with its final C-terminal amino acids facing the ER lumen; the C-terminal GFP tag will thus face the extracellular space if EMD $\Delta 95$ –99-GFP accesses the PM (**Figure 6A**). We tested whether EMD $\Delta 95$ –99's GFP tag is accessible to an anti-GFP antibody applied to the surface of intact cells. In untreated cells, a small amount of EMD $\Delta 95$ –99-GFP (**Figure 6B–D**) is accessible to an anti-GFP antibody, but not to an anti-myc antibody, indicating that EMD $\Delta 95$ –99 is not completely restricted to intracellular membrane compartments under homeostatic conditions. Importantly, the signal from the anti-GFP antibody is specific to cells that express a GFP fusion protein (**Figure 6D–E**). Upon induction of ER stress by THG, the amount of PM-accessible EMD $\Delta 95$ –99-GFP rapidly increases within 2–4 hr, and begins to taper off within 6 hr. This implies that ER stress induces the export of EMD $\Delta 95$ –99-GFP from the NE/ER to the PM as well as its internalization. Importantly, the GFP antibody signal is visible within intracellular puncta, consistent with EMD $\Delta 95$ –99-GFP:antibody conjugates being rapidly internalized into vesicles after PM delivery. Based on the timescale when the levels of EMD $\Delta 95$ –99-GFP begin to significantly decrease at the NE (**Figure 3E–F**), increase in the Golgi (**Figure 4A–D**), transit through the PM (**Figure 6**) and accumulate in lysosomes (**Figure 5F**), we infer that EMD $\Delta 95$ –99-GFP is transported through the secretory pathway to the PM, then internalized and delivered to lysosomes for degradation.

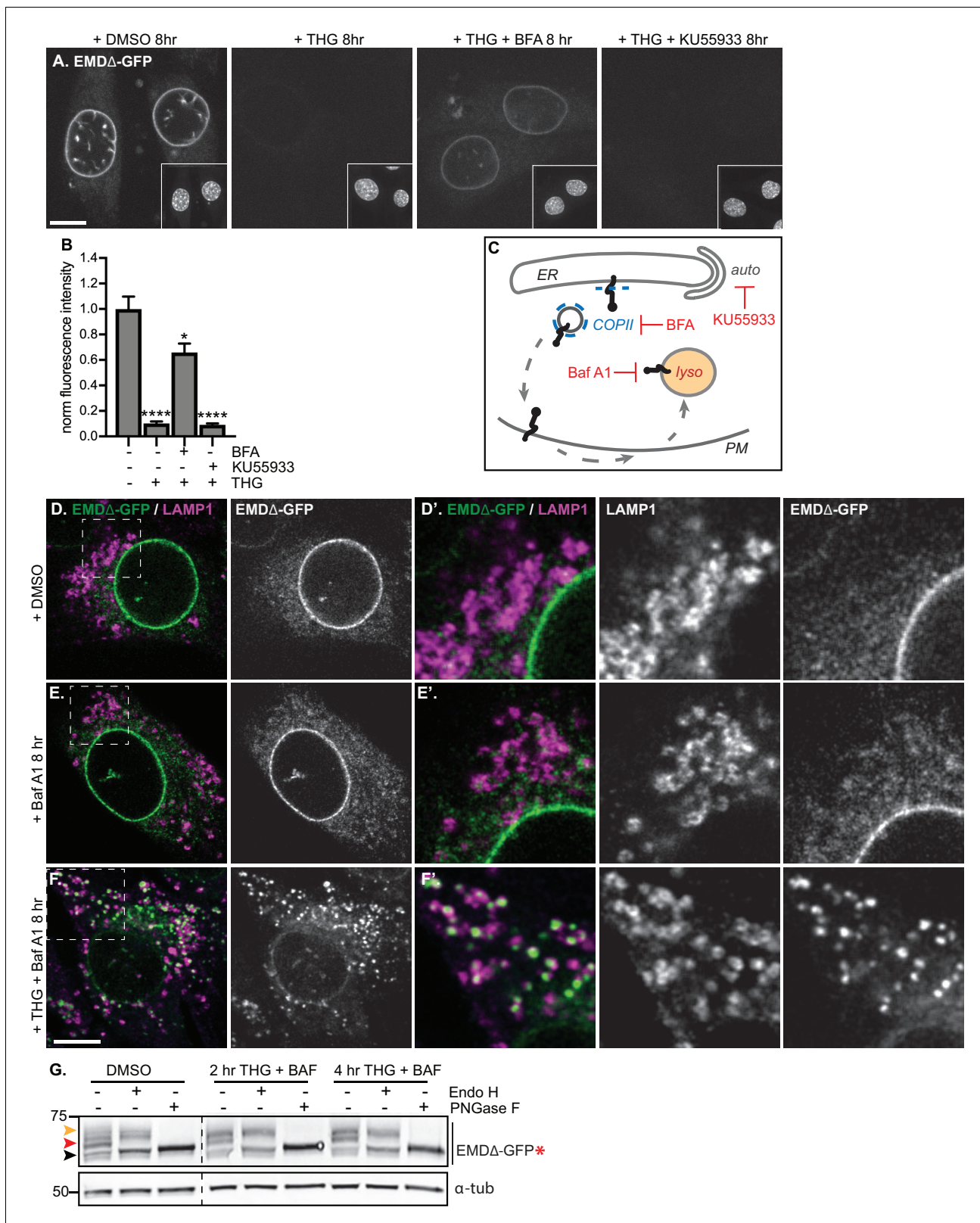


Figure 5. Mutant emerin trafficking is dependent on lysosomal but not autophagosomal function. (A) Representative confocal slices of cells stably expressing EMD Δ -GFP after 8 hr of treatment with DMSO vehicle control, THG, co-treatment with THG and BFA, or co-treatment with THG and KU5933. Insets show nuclei in the same field of view stained with Hoechst. (B) Quantification of NE-localized GFP fluorescence intensity in maximum intensity projections of confocal z series acquired across the conditions shown in (A). Columns indicate average and error bars indicate SEM for N > 56

Figure 5 continued on next page

Figure 5 continued

cells from three independent experiments. **** indicates p -value < 0.0001 compared to untreated (by t-test). (C) Diagram of processes perturbed by KU55933, BFA, and Baf A1 treatment. (D-F) Representative confocal slices of C2C12 cells stably expressing EMD Δ -GFP and costained for LAMP1 after treatment with DMSO vehicle control (D), Baf A1 (E), or co-treatment with THG and Baf A1 (F) for the indicated times. (D'-F') Insets show GFP-LAMP1 colocalization within $\sim 15 \mu\text{m}$ field of view demarcated by dashed rectangles in (D-F). (G) Analysis of EMD Δ -GFP* glycosylation state in cells subjected to treatment with DMSO vehicle control or THG and Baf A1 cotreatments for the times indicated. Red arrowhead indicates EndoH-sensitive glycosylated state of EMD Δ -GFP*; orange arrowhead indicates EndoH-resistant states of EMD Δ -GFP*; black arrowhead indicates deglycosylated EMD Δ -GFP*. α -tubulin shown as loading control. Numbers to left of blots indicate molecular weights in kDa. Scale bars in micrographs indicate $10 \mu\text{m}$. DOI: <https://doi.org/10.7554/eLife.49796.012>

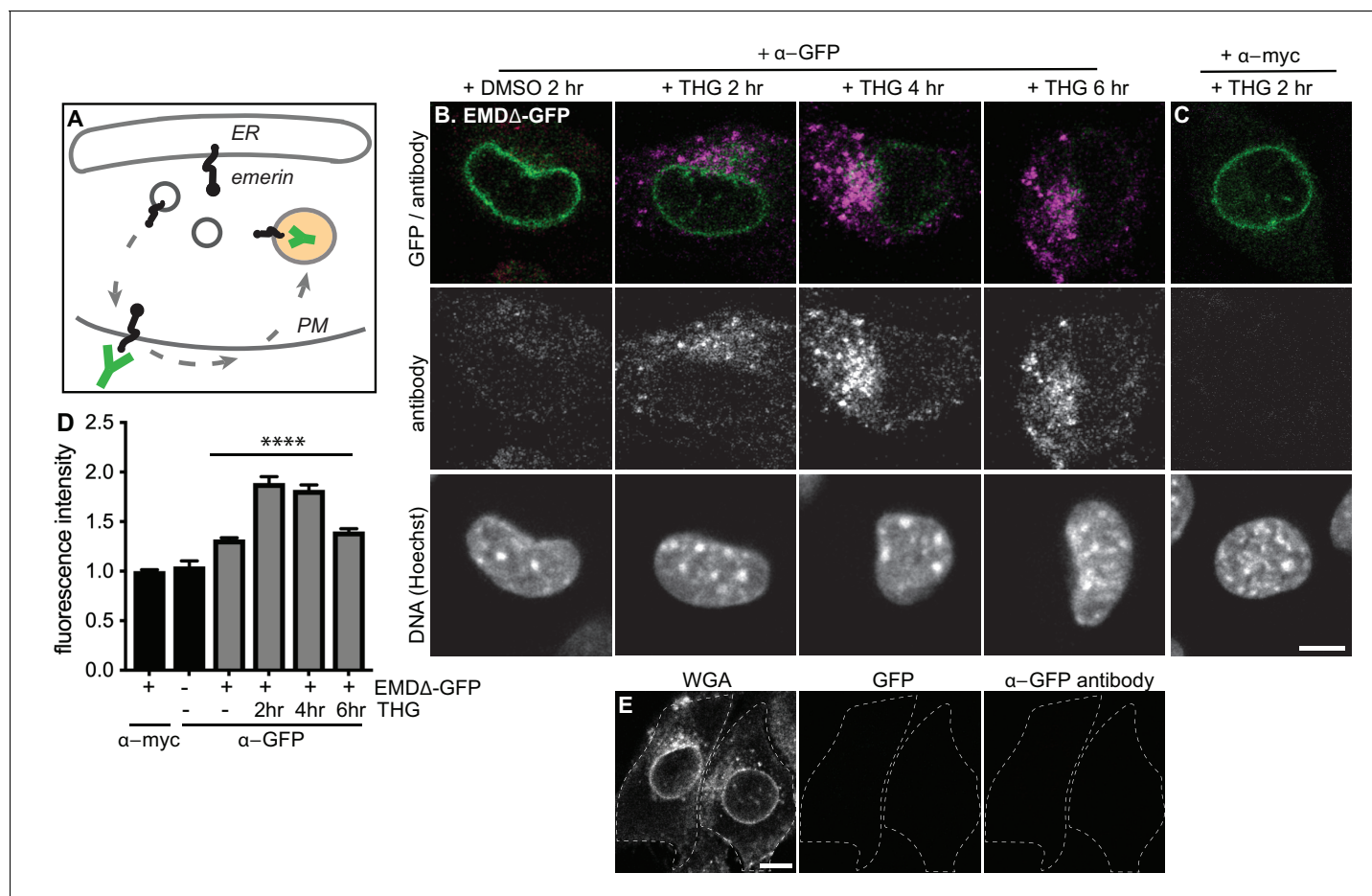


Figure 6. Mutant emerlin traffics through the plasma membrane upon ER stress. (A) Schematic of antibody uptake assay experimental design. If emerlin accesses the plasma membrane (PM), it will be detected by anti-GFP antibody (green), which will bind the surface-exposed GFP tag. (B) Uptake of anti-GFP antibody (magenta) by cells stably expressing EMD Δ -GFP and treated with DMSO vehicle control or THG for 2, 4, or 6 hours. Cells were incubated with anti-GFP antibody for the final hour of these treatment periods before fixation and imaging. (C) Control demonstrating lack of uptake of anti-myc antibody by cells stably expressing EMD Δ -GFP and treated with THG for 2 hours. (D) Quantification of internalized antibody signal in EMD Δ -GFP expressing cells. Columns indicate average and error bars indicate SEM for $N > 235$ cells from 3 independent experiments. **** indicates p -value < 0.0001 (t-test) compared to untreated. (E) Control demonstrating lack of uptake of anti-GFP antibody by untreated C2C12 cells that do not express a GFP fusion protein. WGA is used to define cell boundaries. All images were acquired using the same laser power and detector gain settings. Scale bars in micrographs indicate $10 \mu\text{m}$. See also **Figure 6—figure supplement 1**. DOI: <https://doi.org/10.7554/eLife.49796.013>

The following figure supplement is available for figure 6:

Figure supplement 1. Access of emerlin to the plasma membrane.

DOI: <https://doi.org/10.7554/eLife.49796.014>

Other INM proteins do not undergo stress-dependent clearance

Our findings indicate that EMD Δ 95–99 is subject to proteasome-dependent turnover at the INM (**Figure 2G–H**; **Figure 3A–B**), but can also be rapidly removed from the INM and ER membrane network and targeted for degradation during ER stress. This raises the possibility that additional INM proteins are susceptible to stress-dependent degradation. To address this, we tested the response of additional INM proteins to ER stress induction by THG, to ER export blockage by BFA, and to lysosomal maturation blockage by Baf A1. We selected proteins with distinct topologies and half-lives, including the long-lived polytopic INM protein nurim and the less stable single-pass transmembrane protein Sun2 (see **Figure 1H**, Table S5). Prolonged treatment with THG modestly decreased nurim protein levels and significantly decreased Sun2 protein levels (**Figure 7A–B,D**), likely as a consequence of translational inhibition caused by ER stress (**Harding et al., 1999**). Consistent with this interpretation, the sensitivity of these two proteins tracks with the relative differences in their half-lives (Table S5); nurim has a half-life of ~ 9 days, while Sun2 has a half-life of ~ 3 days in non-dividing cells. Importantly, however, co-incubation with THG and BFA had no effect on either the subcellular localization or abundance of nurim or Sun2 (**Figure 7A–B,D**), indicating that loss of these proteins is not mediated by ER export. Further, neither protein leaves the NE/ER to accumulate in lysosomes when lysosome acidification is blocked by Baf A1 (**Figure 7A', B'**).

We next asked whether wild type EMD was also subject to this pathway. Similarly to EMD Δ 95–99, NE-localized EMD-GFP decreases when stress is induced by THG, but remains stable when stress induction by THG is accompanied by secretory pathway disruption by BFA (**Figure 7C**). ER stress also induces EMD-GFP to enrich in the Golgi (**Figure 4—figure supplement 1**) and access the plasma membrane (**Figure 6—figure supplement 1**). EMD-GFP also accumulates in perinuclear puncta that are likely lysosomes when cells are co-incubated with THG and Baf A1 (**Figure 7C'**). We again engineered an opsin glycosylation site onto the C-terminus of EMD-GFP in order to track movement of EMD through membrane compartments. EMD-WT-GFP* localizes to the NE and responds similarly to ER stress and secretory pathway blockage (**Figure 7—figure supplement 1**). As we observed with EMD Δ 95–99, EMD-WT-GFP* exists predominantly in an Endo H-sensitive modification state in unstressed cells (**Figure 7E–F**, red arrowheads). Higher molecular weight, Endo H-resistant species increase in abundance when cells are co-incubated with THG and CHX (**Figure 7E**, orange arrowhead) or with THG and Baf A1 (**Figure 7F**, orange arrowhead). We thus conclude that wild type EMD is subject to the same stress-induced lysosomal degradation pathway as EMD Δ 95–99. However, when EMD-GFP's response to THG is tracked over time, it is clear that displacement of wild type EMD from the NE proceeds significantly more slowly than displacement of EMD Δ 95–99 (**Figure 8B,D**). This indicates that stress-dependent trafficking out of the INM is selective to variants of EMD, and that intrinsic features of EMD control its clearance from the NE/ER and targeting into lysosomes.

A signal within emerins' LEM domain is required for stress-dependent export

Why are EMD variants selectively targeted for stress-dependent clearance from the INM and ER? We considered functional domains that might be involved in responding to ER stress. EMD is a tail-anchored protein with a ~ 10 amino acid tail that protrudes into the ER lumen (**Figure 3A**). This short sequence lacks any known motifs for engaging with proteins within the ER lumen. EMD's nucleoplasmic domain includes an N-terminal LEM domain and an internal lamin A-binding region (**Figure 3A**). Emerin relies on lamin A for targeting to the INM (**Vaughan et al., 2001**) but we noted that in *Imna* -/- MEFs, EMD-GFP remained stably expressed even while mislocalized to the peripheral ER (**Figure 8—figure supplement 2**). The small deletion within EMD Δ 95–99 falls within the lamin A-binding domain, but does not appear to affect the protein's affinity for the lamina as judged by FRAP (**Figure 2—figure supplement 1**), even though this variant responds more potently than wild type EMD to ER stress (**Figure 8D**). Taken together, these observations indicate that dissociation from the lamina is not sufficient to promote clearance of EMD from the NE/ER membrane system.

We next evaluated whether interactions mediated by the LEM domain could contribute to stress-dependent EMD export. The LEM domain (**Figure 3A**) is a protein fold that binds with high affinity to the soluble nucleoplasmic protein BAF (**Lee et al., 2001**). We deleted this domain and queried the effects on EMD localization and trafficking. When expressed within unperturbed cells, EMD Δ LEM

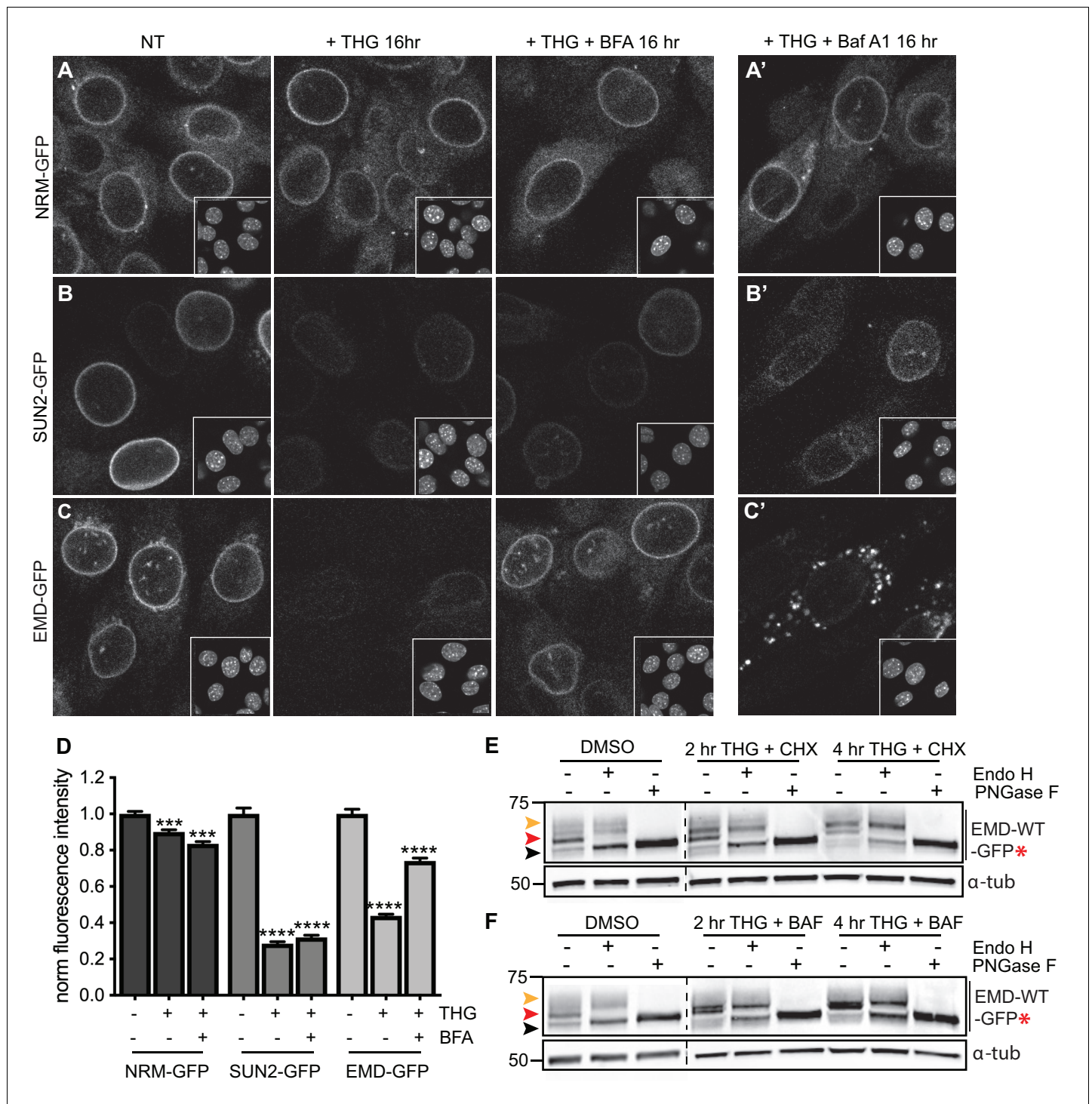


Figure 7. Emerin, but not other INM proteins, undergoes stress-dependent clearance from the NE and ER and accesses lysosomes. (A-C) Representative confocal slices of cells stably expressing NRM-GFP (A), Sun2-GFP (B), or EMD-GFP (C) after 16 hr of treatment with DMSO vehicle control, THG, or co-treatment with THG and BFA. Insets show nuclei in the same ~ 50 μ m field of view stained with Hoechst. (A'-C') Representative confocal slices of cells co-treated with THG and Baf A1. All images were acquired using the same laser power and detector gain settings. (D) Quantification of GFP fluorescence intensity at the NE in maximum intensity projections of confocal z series acquired across conditions represented in (A-C). Columns indicate average and error bars indicate SEM for N > 690 cells from three independent experiments. **** indicates p-value < 0.0001 compared to untreated (t-test). (E-F) Analysis of EMD-WT-GFP* glycosylation state in cells subjected to treatment with DMSO vehicle control or THG and CHX (E) or THG and Baf A1 (F) cotreatments for the times indicated. Red arrowhead indicates EndoH-sensitive glycosylated state of EMD-WT-GFP*; orange arrowhead indicates EndoH-resistant states of EMD-WT-GFP*; black arrowhead indicates deglycosylated EMD-WT-GFP*. α -tubulin

Figure 7 continued on next page

Figure 7 continued

shown as loading control. Numbers to left of blots indicate molecular weights in kDa. Scale bars in micrographs indicate 10 μ m. See also **Figure 7—figure supplement 1**.

DOI: <https://doi.org/10.7554/eLife.49796.015>

The following figure supplement is available for figure 7:

Figure supplement 1. Glycosylation reporter variants are destabilized by ER stress and recovered by BFA treatment.

DOI: <https://doi.org/10.7554/eLife.49796.016>

exhibited normal enrichment in the NE (**Figure 8C**), consistent with its ability to bind the lamina independently of the LEM domain. However, we observed that this mutant was less responsive than other EMD variants to ER stress induction; NE-localized EMD Δ LEM was clearly detectable over several hours of THG treatment and was significantly less sensitive than full-length EMD to ER stress (**Figure 8C–E**). We surmise that the eventual loss of EMD Δ LEM results from translational inhibition resulting from ER stress (**Harding et al., 1999**) and degradation by alternative pathways. Consistent with the interpretation that the LEM domain mediates post-ER trafficking, co-incubation of EMD Δ LEM-expressing cells with THG and BFA or Baf A1 each had no effect on protein levels or localization (**Figure 8F–H**). These results suggest that without the LEM domain, EMD does not access post-ER compartments. To directly evaluate this, we generated a glycosylation-reporting variant, EMD Δ LEM-GFP*, with a glycosylation consensus site at the luminal C terminus. In contrast to variants of EMD with an intact LEM domain, EMD Δ LEM-GFP* accumulates only Endo H-sensitive modifications and remains equivalently Endo H-sensitive during ER stress and lysosome blockage (**Figure 8I–J**, red arrowheads). Altogether, these data indicate that a signal within emerin's LEM domain enables selective export from the ER under stress conditions.

Discussion

In this work, we applied a dynamic proteomic strategy to define organelle-wide trends in protein turnover across the NE/ER membrane network in mammalian cells. While the INM is separated from the bulk ER by the selective barrier of the NPC, we observe no difference in global protein turnover rates between the ER and INM compartments or any correlation between INM protein size and turnover kinetics. This, along with specific visualization of mature INM proteins by RITE tagging and microscopy (**Figure 2**) and previous studies (**Tsai et al., 2016**), suggests that turnover of INM proteins can be effectively achieved in situ.

Moving forward with the rapidly turned over INM protein EMD as a model substrate for dissecting INM protein turnover, we identified an even less stable, EDMD-linked variant of EMD as an ideal substrate for sensitively probing INM protein turnover pathways. We noted that turnover of maturely folded EMD and EMD Δ 95–99 exhibits proteasome dependence at the INM (**Figure 2F–H**; **Figure 3A**), while nascent EMD Δ 95–99 accumulates in multiple cellular compartments when the proteasome is inhibited (**Figure 3A**, fourth panel). Taken together, these observations lead us to infer that mature EMD variants and potentially other INM proteins can be turned over in situ at the INM by a pathway that terminates in proteasomal degradation, while immature EMD variants (and potentially other INM proteins) are also subject to co-translational quality control that terminates in proteasomal degradation. As proteasomal inhibition and p97 inhibition each stabilize EMD Δ 95–99 (**Figure 3B**), we expect that EMD Δ 95–99 is an ERAD client under some conditions.

Surprisingly, however, we also find that EMD can be selectively shunted to an alternative turnover pathway under conditions of acute ER stress. This pathway is rapidly induced by ERAD blockage or by pharmacological induction of acute ER protein folding stress (**Figure 3**) and requires ER export (**Figures 3 and 4**). Notably, changes to EMD Δ 95–99 localization and levels are apparent at a time-scale shorter than the normal half-life of EMD Δ 95–99, within 2–4 hr of ER stress induction. Based on the transient appearance of EMD Δ 95–99 at the PM (**Figure 6**) and its accumulation in lysosomes (**Figure 5**), we conclude that EMD transits through the secretory pathway and is then internalized into lysosomes. While our data indicate that a significant proportion of EMD leaves the NE/ER during ER stress, we cannot rule out the possibility that ERAD-mediated degradation of some proportion of EMD takes place within the NE/ER network in parallel to the lysosome-mediated pathway

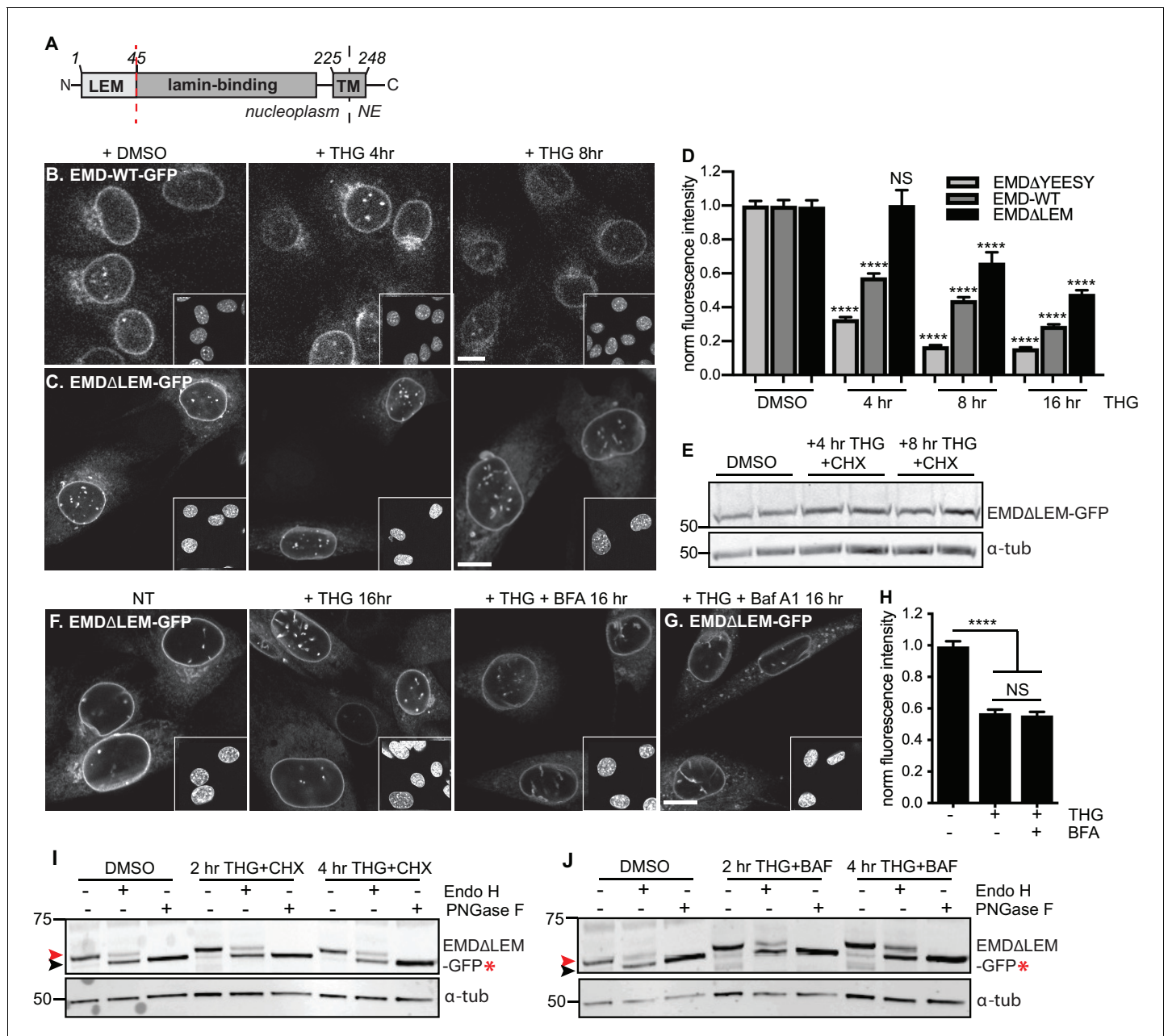


Figure 8. A signal within emerin's. LEM domain is required for stress-dependent clearance from the NE and ER (A) Diagram of emerin domain organization with N-terminal LEM domain deletion indicated (amino acids 1-45). (B-C) Representative confocal slices of C2C12 cells stably expressing EMD-WT-GFP (B) or EMD Δ LEM-GFP (C) after treatment with DMSO vehicle control or THG for the indicated times. Insets show nuclei in the same ~50 μ m field of view stained with Hoechst. (D) Quantification of EMD Δ 95-99-GFP (as also shown in Figure 3F), EMD-WT-GFP, and EMD Δ LEM-GFP fluorescence intensity at the NE in maximum intensity projections of confocal z series acquired across the timecourse shown in (B-C). Columns indicate average and error bars indicate SEM for N > 146 cells from 3 independent experiments. **** indicates p-value < 0.0001 compared to untreated (t-test). (E) Western blot of EMD Δ LEM-GFP in cells treated with DMSO vehicle control or co-treated with THG and CHX for the indicated times. (F-G) Representative confocal slices of C2C12 cells stably expressing EMD Δ LEM-GFP after treatment with (F) DMSO vehicle control, THG, THG + BFA, or (G) THG + Baf A1. (H) Quantification of GFP fluorescence intensity at the NE across the conditions shown in (F). Columns indicate average and error bars indicate SEM for N > 776 cells from 3 independent experiments. **** indicates p-value < 0.0001 compared to untreated (t-test). (I-J) Analysis of EMD- Δ LEM-GFP* glycosylation state in cells subjected to treatment with DMSO vehicle control or THG and CHX (I) or THG and Baf A1 (J) cotreatments for the times indicated. Red arrowhead indicates EndoH-sensitive glycosylated state of EMD Δ LEM-GFP*; black arrowhead indicates deglycosylated EMD Δ LEM-GFP*. α -tubulin shown as loading control. Numbers to left of blots indicate molecular weights in kDa. Scale bars in micrographs indicate 10 μ m. See also **Figure 8—figure supplements 1 and 2.**

DOI: <https://doi.org/10.7554/eLife.49796.017>

Figure 8 continued on next page

Figure 8 continued

The following figure supplements are available for figure 8:

Figure supplement 1. Stability of EMD Δ LEM-GFP over time of cycloheximide treatment.

DOI: <https://doi.org/10.7554/eLife.49796.018>

Figure supplement 2. Emerin is mislocalized to the ER, but not degraded in *Imna* $-/-$ MEFs.

DOI: <https://doi.org/10.7554/eLife.49796.019>

that we have identified. Nonetheless, this dynamic and selective removal of an INM protein is quite surprising and is inconsistent with models of the INM as a terminal depot for its resident proteins.

Our findings have some intriguing parallels to the fate of a misfolded variant of the GPI-anchored prion protein, PrP, during ER stress (*Satpute-Krishnan et al., 2014*). PrP is normally targeted to the PM, but a misfolded variant is retained within the ER by persistent association with protein folding chaperones. Similarly to what we observe for an INM protein, ER stress induces the rapid export of misfolded PrP through the secretory pathway, followed by transit through the PM and internalization and delivery to lysosomes for degradation. This mode of clearance has been referred to as rapid ER stress-induced export, or RESET (*Satpute-Krishnan et al., 2014*).

There are several notable contrasts between PrP's export from the peripheral ER and EMD's export from the INM and ER. For instance, the topologies of PrP and EMD are quite disparate. As a GPI-anchored protein, misfolded PrP faces the lumen of the ER, and an interaction between PrP and Tmp21, a sorting adaptor for luminal proteins, controls RESET (*Satpute-Krishnan et al., 2014*). Misfolded PrP remains associated with additional luminal ER-derived proteins during its transit through the secretory pathway, and these associations appear to enable recognition of misfolded PrP at the cell surface for internalization (*Zavodszky and Hegde, 2019*). In contrast, EMD is a tail-anchored protein, and interactions mediated by EMD's nucleoplasmic-facing LEM domain (*Figure 8*) control its stress-dependent clearance. We do not yet know whether EMD remains associated with other proteins as it transits through the secretory pathway, or what role those associations might play in targeting EMD for degradation.

PrP and EMD also exhibit distinct subcellular localization when not undergoing RESET. Misfolded PrP is retained in the ER network until RESET is initiated, while EMD is enriched in the INM and associated with the nuclear lamina. Importantly, EMD is small enough (~25 kDa) to diffuse freely across the NPC, meaning that it may release INM-localized binding partners and sample the ER with some frequency. This spatial separation between EMD's normal site of enrichment and its site of ER export may explain the longer timescale of RESET for EMD (2–4 hr) compared to ER-localized misfolded PrP (~1 hr) (*Satpute-Krishnan et al., 2014*).

Finally, PrP and EMD variants exhibit clear differences in selectivity for the RESET pathway. Only misfolded, ER-retained mutants of PrP are subject to RESET. On the other hand, both wild type EMD (*Figure 7*) and a less stable disease-linked variant (EMD Δ 95–99) are subject to stress-dependent clearance, although EMD Δ 95–99 is more rapidly cleared from the NE and ER. Both EMD variants appear functional until ER stress is induced, as judged by their localization and affinity for the INM (*Figure 3, Figure 2—figure supplement 1*). This suggests that clearance of EMD from the NE/ER is not strictly contingent on protein misfolding.

We find that selective, stress dependent clearance of EMD depends on its 45-amino acid LEM domain. LEM domains bind dynamically to the small soluble protein BAF, which exists in both nuclear and cytoplasmic pools (*Shimi et al., 2004*). While glycosylation reporters indicate that EMD variants also exit the NE/ER with some frequency under homeostatic conditions (*Figure 3H, Figure 7E–F*), this is completely abolished by deletion of the LEM domain (*Figure 8*). One model that could explain the dichotomy between LEM-mediated BAF binding and LEM-mediated ER export is that BAF and ER export-promoting factor(s) bind competitively to the same surface of EMD's LEM domain (*Figure 9*). It could be that acute ER stress is relayed to EMD via a structural reorganization or post-translational modification that disrupts the LEM:BAF interface. It is possible that this system could be used to rapidly remove EMD in response to ER stress and potentially other physiological stressors. This could in turn rapidly inhibit the normal functions of EMD at the INM, including participating in mechanosensitive signaling pathways (*Guilluy et al., 2014*) and contributing to the scaffolding of heterochromatic domains at the nuclear periphery (*Demmerle et al., 2013*).

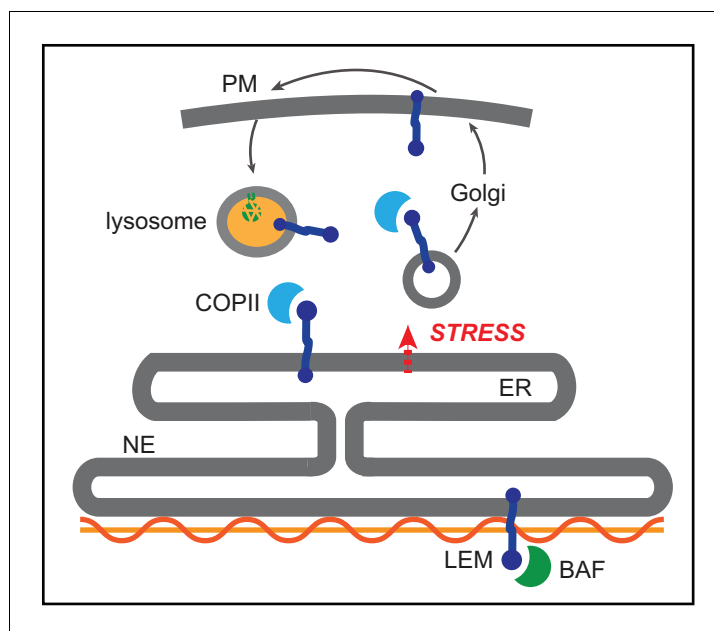


Figure 9. Competition model for emerin sorting via its LEM domain competitively binding to BAF or to the ER export machinery.

DOI: <https://doi.org/10.7554/eLife.49796.020>

Overall, our findings indicate that the INM can be rapidly remodeled in response to environmental stimuli, and that the function of the INM protein EMD may be dynamically controlled by integration of environmental inputs via its LEM domain.

Notably, muscular dystrophy and cardiomyopathy diseases are caused by loss-of-function mutations to EMD, many of which further destabilize the protein (Bonne and Quijano-Roy, 2013; Fairley et al., 1999). We find evidence that a muscular dystrophy-linked EMD variant (EMD Δ 95–99) is more rapidly degraded under acute stress conditions, suggesting that an overzealous response to ER stress could contribute to the pathogenesis of EDMD. EMD is broadly expressed (Uhlen et al., 2015), but mutations predominantly affect muscle tissues. Intriguingly, skeletal muscle undergoes significant ER stress both during development and during normal function (Deldicque et al., 2012). We speculate that these features of muscle physiology may make muscle-localized EMD mutants especially vulnerable to ER stress-induced degradation.

Materials and methods

Key resources table

Reagent type (species) or resource	Designation	Source or reference	Identifiers	Additional information
Gene (<i>Mus musculus</i>)	emerin		NCBI RefSeq NM_007927	
Gene (<i>Mus musculus</i>)	nurim		NCBI RefSeq NM_134122	
Gene (<i>Mus musculus</i>)	Sun2		NCBI RefSeq NM_001205346	
Cell line (<i>Mus musculus</i>)	C2C12	ATCC	CRL-1772	

Continued on next page

Continued

Reagent type (species) or resource	Designation	Source or reference	Identifiers	Additional information
Cell line (<i>Homo sapiens</i>)	U-2-OS	ATCC	HTB-96	
Recombinant DNA reagent (plasmid)	pQCXIB vector	Campeau et al. (2009) Addgene		Retroviral construct for stable expression
Recombinant DNA reagent (plasmid)	Myc/FLAG RITE vector	Toyama et al. (2019)		Lentiviral construct for stable expression of RITE-tagged protein
Recombinant DNA reagent (plasmid)	pQCXIB emerin-GFP	This paper		Retroviral construct for stable expression
Recombinant DNA reagent (plasmid)	pQCXIB emerin-D95-99-GFP	This paper		Retroviral construct for stable expression
Recombinant DNA reagent (plasmid)	pQCXIB emerin-DLEM-GFP	This paper		Retroviral construct for stable expression
Recombinant DNA reagent (plasmid)	pQCXIB emerin-GFP-SSNKTVD	This paper		Retroviral construct for stable expression
Recombinant DNA reagent (plasmid)	pQCXIB emerin-Δ95-99-GFP-SSNKTVD	This paper		Retroviral construct for stable expression
Recombinant DNA reagent (plasmid)	pQCXIB emerin-ΔLEM-GFP-SSNKTVD	This paper		Retroviral construct for stable expression
Recombinant DNA reagent (plasmid)	pQCXIB Sun2-GFP	This paper		Retroviral construct for stable expression
Recombinant DNA reagent (plasmid)	pQCXIB nurim-GFP	This paper		Retroviral construct for stable expression
Recombinant DNA reagent (plasmid)	Emerin-RITE	This paper		Lentiviral construct for stable expression of RITE-tagged protein
Recombinant DNA reagent (plasmid)	Nurim-RITE	This paper		Lentiviral construct for stable expression of RITE-tagged protein

Continued on next page

Continued

Reagent type (species) or resource	Designation	Source or reference	Identifiers	Additional information
Recombinant DNA reagent (plasmid)	Emerin-Δ95–99-RITE	This paper		Lentiviral construct for stable expression of RITE-tagged protein
Antibody	Rabbit polyclonal anti-emerin	Santa Cruz Biotechnology	Sc-15378	WB (1:1000)
Antibody	GFP	Abcam	ab290	Ab uptake (1:500); WB (1:1000)
Antibody	Mouse monoclonal anti-FLAG	Sigma-Aldrich	F1804	IF (1:1000)
Antibody	Mouse monoclonal anti-Myc	Cell Signaling	2233	IF (1:1000); Ab uptake (1:500)
Antibody	Mouse monoclonal anti-tubulin	Sigma-Aldrich	T5168	WB (1:2500)
Antibody	giantin	BioLegend	PRB-114C	IF (1:1000)
Antibody	LAMP1	Abcam	ab24170	IF(1:100)
Other	Alexa-647 WGA	Life Technologies	W32466	IF (5 ug/ml)
Commercial assay or kit	PNGase F	NEB	P0704	
Commercial assay or kit	Endo H	NEB	P0702	
Chemical compound, drug	Thapsigargin	Thermo Fisher	T7459	Used at 100 nM
Chemical compound, drug	MG132	Cayman Chemical	1211877-36-9	Used at 10 uM
Chemical compound, drug	Bafilomycin A1	BioVotica	BVT-0252	Used at 100 nM
Chemical compound, drug	Brefeldin A	Tocris	1231	Used at 2.5 uM
Chemical compound, drug	Leupeptin	Sigma-Aldrich	L5793	Used at 125 uM
Chemical compound, drug	cycloheximide	Sigma-Aldrich	C-7698	Used at 200 ug/ml
Other	¹³ C ₆ -Lysine	Cambridge Isotopes	CLM-2247	
Other	¹³ C ₆ , ¹⁵ N ₄ -Arginine	Cambridge Isotopes	CNLM-539	
Other	Lysine/arginine free DMEM	Thermo Fisher	88364	
Other	Dialyzed fetal bovine serum	Thermo Fisher	26400044	
Other	Hoechst stain	Molecular Probes	H1399	Used at 10 ug/ml

Continued on next page

Continued

Reagent type (species) or resource	Designation	Source or reference	Identifiers	Additional information
Recombinant DNA reagent (plasmid)	UBE2G1 miR-E LT3GEPiR	<i>Knott et al., 2014</i>		TGCTGTTGACAGTG AGCGAAAGACAGC TGGCAGAACT CAATAGTGAAGCCA CAGATGTATTGA GTTCTGCCAGCT GTCTTCTGCC TACTGCCTCGGA
Recombinant DNA reagent (plasmid)	UBE2G2 miR-E LT3GEPiR	<i>Knott et al., 2014</i>		TGCTGTTGACA GTGAGCGAACC GGAGCAGTTCTATAAG ATAGTGAAGCCACAGA TGTATCTTATAGAA CTGCTCCCGGTCTG CCTACTGCCTCGGA
Recombinant DNA reagent (plasmid)	UBE2J1 miR-E LT3GEPiR	<i>Knott et al., 2014</i>		TGCTGTTGACA GTGAGCGAAAGGTTG TCTACTTCA CCAGATAGTGA AGCCACAGATGTATC TGGTGAAGTAGACAACC TTCTGCCTA CTGCCTCGGA
Recombinant DNA reagent (plasmid)	MARCH6 miR-E LT3GEPiR	<i>Knott et al., 2014</i>		TGCTGTTGACAGTG AGCGACTGGATC TTCATTCTTATTTA TAGTGAAGCCACA GATGTATAAATAAGA ATGAAGATCCA GCTGCCTAC TGCTCGGA
Software, algorithm	Fiji	https://fiji.sc/		
Software, algorithm	RStudio	https://rstudio.com/		

SILAC labeling

SILAC labeling was performed as a pulse-chase (*Ong and Mann, 2006*). Proliferating C2C12 mouse myoblasts were subcultured for > 5 population doublings in culture medium containing stable heavy isotopes of lysine and arginine ($^{13}\text{C}_6$ -Lysine, $^{13}\text{C}_6$, $^{15}\text{N}_4$ -Arginine) to completely label the cellular proteome. Cells were grown in SILAC-formulated DMEM lacking lysine and arginine and supplemented with 20% dialyzed FBS, penicillin/streptomycin, and SILAC amino acids. Complete label incorporation was verified by LC-MS/MS. Myoblasts were then grown to confluency and switched to differentiation medium containing heavy isotopes for 5 days to induce myotube differentiation. Differentiation medium contained SILAC DMEM, 2% dialyzed FBS, penicillin/streptomycin, and SILAC amino acids. Media was refreshed every other day. After differentiation, the mature myotube culture was switched to low serum differentiation medium containing the normal isotopes of lysine and arginine: $^{12}\text{C}_6$ -Lysine, $^{12}\text{C}_6$, $^{14}\text{N}_4$ -Arginine for 1–3 days.

Crude nuclear extracts were prepared similarly to previous work (*Buchwalter and Hetzer, 2017; Schirmer et al., 2003*). Cells were harvested by scraping into PBS, then swollen in hypotonic lysis buffer (10 mM potassium acetate, 20 mM Tris acetate pH 7.5, 0.5 mM DTT, 1.5 mM MgCl₂, and protease inhibitors), followed by mechanical lysis through a 25-gauge needle and syringe. The nuclei were pelleted and the supernatant (containing cytosol) was decanted. Nuclei were then resuspended in buffer containing 10 mM Tris pH 8.0, 10% sucrose, 1 mM DTT, 0.1 mM MgCl₂, 20 ug/ml DNase I, and 1 ug/ml RNase I. After nuclease treatment, nuclei were layered on top of a 30% sucrose cushion and pelleted. Crude nuclei were then extracted in 10 mM Tris pH 8, 1% n-octyl glucoside, 400 mM NaCl, and 1 mM DTT, and extracts and pellets were prepared separately for liquid chromatography-mass spectrometry.

Lc-ms/MS

Samples were denatured in 8M urea/100 mM TEAB, pH 8.5; reduced with TCEP; alkylated with chloroacetamide; and digested overnight with trypsin. Digestion was quenched with 5% formic acid. Detergent was removed from pulse-labeled SILAC samples with SCX tips (EMD Millipore). Samples were run on a Thermo Orbitrap Fusion Tribrid MS/MS with CID fragmentation. The digest was injected directly onto a 30 cm, 75 μ m ID column packed with BEH 1.7 μ m C18 resin. Samples were separated at a flow rate of 200 nl/min on a nLC 1000. Buffer A and B were 0.1% formic acid in water and acetonitrile, respectively. A gradient of 1–25% B over 160 min, an increase to 35% B over 60 min, an increase to 90% B over another 10 min and a hold at 90%B for a final 10 min of washing was used for a total run time of 240 min. The column was re-equilibrated with 20 μ l of buffer A prior to the injection of sample. Peptides were eluted directly from the tip of the column and nanosprayed into the mass spectrometer by application of 2.5 kV voltage at the back of the column. The Orbitrap Fusion was operated in data dependent mode. Full MS1 scans were collected in the Orbitrap at 120K resolution with a mass range of 400 to 1500 m/z and an AGC target of 4e. The cycle time was set to 3 s, and within this 3 s the most abundant ions per scan were selected for CID MS/MS in the ion trap with an AGC target of 1e and minimum intensity of 5000. Maximum fill times were set to 50 ms and 100 ms for MS and MS/MS scans, respectively. Quadrupole isolation at 1.6 m/z was used, monoisotopic precursor selection was enabled, charge states of 2–7 were selected and dynamic exclusion was used with an exclusion duration of 5 s.

Analysis of proteomic data

Peptide and protein identification, quantification, and analysis were performed with Integrated Proteomics Pipeline (IP2) (Integrated Proteomics Applications; www.integratedproteomics.com). Tandem mass spectra were extracted from raw files using RawConverter (He et al., 2015) and searched with ProLUCID (Xu et al., 2015) against the mouse UniProt database (ID). The search space included all fully tryptic and half-tryptic peptide candidates. Carbamidomethylation on cysteine was allowed as a static modification. Data were searched with 50 ppm precursor ion tolerance and 600 ppm fragment ion tolerance. Data were filtered to 10 ppm precursor ion tolerance post-search. Identified proteins were filtered using DTASelect (Tabb et al., 2002) and utilizing a target-decoy database strategy to control the false discovery rate to 1% at the protein level.

Census2 (Park et al., 2014) was used for quantitative analysis of SILAC-labeled peptides. Peptides were subjected to stringent quality control criteria before inclusion in half-life determination analyses. Firstly, any peptide with a profile score < 0.8 was discarded. Secondly, peptides were filtered based on the extent of correlation between the heavy and light chromatograms, which is quantified as a regression score in Census. Peptides with extreme area ratios (less than 0.111 or greater than 9) were retained only if their regression score was > 0. Peptides with intermediate area ratios (between 0.111 and 9) were retained only if their regression score was > 0.8.

Half-life calculation

For estimation of protein half-lives, we restricted our analysis to peptides that were detected in at least three timepoints. 1685 proteins passed this criterion with at least one peptide; individual peptides and protein-level data are reported in Tables S1 and S2, respectively. Area ratio values were transformed into % old values using the following equation:

$$\%old = 100 * (1/(1 + AR))$$

And individual peptides were fit to a line corresponding to the following equation:

$$\ln(\%old) = kt + a$$

Individual peptide fits with $r^2 > 0.8$ and values of $k < 0$ were retained for protein-level estimation of half-life. The slope of the fit for all peptides detected were averaged to produce an average value and standard deviation at the protein level. These average slope values were converted to half-life estimates using the equation below.

$$T_{1/2} = -\ln(2)/k$$

These values are reported in Table S3 for 1677 proteins. While calculated half-lives range from ~0.33 days to ~30 days, we note that half-lives at either extreme should be considered rough estimates of protein stability. For illustration, we have included example fits for proteins in Figure S1 with predicted half-lives of 0.5 day, 1 day, 2 days, 4 days, 8 days, and 16 days. Linear regression predicts half-life well under conditions where a line can be fitted with high fidelity and a non-zero slope is detectable. We note the good performance and clear distinctions in slope for proteins with predicted half-lives ranging from 1 to 8 days, and observed more frequent deviations in linearity at the low extreme (predicted $T_{1/2} < 1$ day) and slopes approaching zero at the high extreme (predicted $T_{1/2} > 8$ days). We expect that these factors limit the precision of half-life determination below 1 day and above 8 days from a 3 day timecourse. Shorter or longer timecourses would be required to investigate turnover at these timescales.

The TMHMM server (*Krogh et al., 2001*) was used to define the positions of transmembrane domains in INM proteins and infer extraluminal domain sequences.

Plasmid construction

All emerlin constructs are based on the emerlin sequence from mouse (Uniprot ID O08579); all nurim constructs based on the nurim sequence from mouse (Uniprot ID Q8VC65); and all Sun2 constructs based on the Sun2 sequence from mouse (Uniprot ID Q8BJS4). Emerlin, Sun2, and nurim were each C-terminally tagged with GFP by stitching PCR (*Heckman and Pease, 2007*), where each open reading frame was amplified with the start codon included and the stop codon omitted, while GFP was amplified with its start codon omitted and stop codon included. Primersets were designed with overhangs including homology between each ORF and GFP, so that a second round of PCR with flanking primers and the first two PCR products used as templates generates an ORF-GFP fusion. EMD Δ 95–99 was generated by Quickchange mutagenesis of the emerlin-GFP sequence followed by sequence verification. EMD Δ LEM-GFP was constructed by stitching PCR of emerlin nucleic acid sequence 136–777 corresponding to residues 46–258 of emerlin protein with the stop codon omitted. A new ATG start codon was introduced by PCR, and the C-terminal GFP tag introduced by stitching PCR. All ORFs were introduced into the pQCXIB vector (*Campeau et al., 2009*) for retroviral delivery and constitutive expression under a CMV promoter by Gateway cloning.

INM-RITE tag plasmids were constructed as described in *Toyama et al. (2019)*. ORFs of interest were introduced into the FLAG/myc-RITE or myc/FLAG-RITE plasmid backbones, then the entire ORF-RITE construct was amplified and recombined into a pDONR207 Gateway entry vector, followed by recombination into the pQCXIB retroviral vector for constitutive mammalian expression.

Glycosylation reporter plasmids were constructed by introducing a 21 base-pair sequence encoding the glycosylation acceptor site SSNKTVD within a 3' PCR primer for amplification of EMD-WT-GFP, EMD Δ YEESY-GFP, and EMD Δ LEM-GFP. The resulting PCR product was inserted into the pQCXIB vector by Gateway cloning. Sequence verified clones were used for stable cell line generation.

UBE2G1, UBE2G2, UBE2J1, and MARCH6 miR-E inducible RNAi plasmids were constructed as described in *Fellmann et al. (2013)*. Validated shRNA sequences with the highest score for targeting mouse UBE2G1, UBE2G2, UBE2J1, and MARCH6 were selected from the shERWOOD database (www.sherwood.cshl.edu), and ~100 bp oligonucleotides with the corresponding sequence were synthesized. This sequence was amplified by PCR using degenerate primers with XhoI and EcoRI restriction sites. The PCR was digested with XhoI and EcoRI, gel purified, and ligated into the LT3GEPIR lentiviral vector for doxycycline-inducible RNAi expression with GFP reporter fluorescence. The LT3GEPIR vector was the kind gift of Johannes Zuber.

Cell line generation

GFP-tagged cell lines were generated in C2C12 mouse myoblasts. Low-passage C2C12 cells were obtained from ATCC, and identity was validated by a functional assay: cells were grown to confluency, switched to low serum medium for several days, and evaluated for the formation of multinucleated myotubes. Parallel cultures of C2C12 cells were infected with virus encoding GFP fusion proteins. 293 T cells were transfected with delivery vectors and viral packaging vectors for retroviral or lentiviral production. Conditioned media were collected 48–72 hr after transfection and applied to low-passage C2C12 cells in the presence of polybrene. Integrated clones were selected using the

relevant antibiotic selections for each vector backbone. Fluorescent cell populations were isolated by FACS. The resulting stable GFP-expressing C2C12 cell lines were tested to verify the absence of mycoplasma contamination. miR-E RNAi cell lines were generated in U2OS cells. U2OS cells were obtained from ATCC and were periodically tested for mycoplasma contamination. EMD Δ 95–99-GFP was introduced by retroviral infection and FACS sorted as described above. miR-E RNAi expression vectors were then introduced into these stable cell lines by lentiviral infection.

RITE tag switching

RITE tag switching experiments were performed in quiescent C2C12 cells stably expressing RITE-tagged INM proteins. C2C12s were grown in Ibidi chamber slides and induced to enter quiescence as previously described (Zhang *et al.*, 2010) by growing C2C12 myoblasts to ~75% confluence, washing twice in warm PBS, and switching to quiescent medium (DMEM without methionine, 2% FBS, and pen-strep). Cells were maintained in quiescent medium for 3 days with media changes every other day before initiation of RITE timecourses. To induce tag exchange, concentrated adenovirus expressing Cre recombinase was added to the culture medium. Tag switching was initiated at the indicated timepoints such that the entire slide containing all time points could be fixed, stained, imaged, and quantified in parallel. To quantify loss of 'old' RITE-tagged protein over time, intensity per unit area of the 'old' tag was quantified across all conditions. Background measurements were taken from cell-free regions of the imaging dish and subtracted from all signals as a background correction. All signals were then normalized to the day 0 timepoint (no tag switch).

Antibody uptake assays

For antibody uptake assays, cells were pre-treated with drugs for the indicated times, then incubated in medium containing antibody, drug, and 125 μ M leupeptin for 1 hr before fixation in paraformaldehyde and staining. Cells were stained with Alexa Fluor-conjugated secondary antibody to visualize internalized primary antibody:GFP conjugates. Cell surfaces were stained with Alexa Fluor-conjugated WGA; the WGA signal was used as a guide for outlining individual cells and quantifying internalized antibody fluorescence.

Preparation of protein lysates and western blotting

Cells were washed in PBS, then lysed directly in plates in PBS lysis buffer (PBS supplemented with 1% Triton-X-100, 0.1% SDS, and protease inhibitors). Cells were further lysed by passage through a 25-gauge needle. Protein concentrations were quantified by BCA assay, and ~20 μ g of total protein was loaded per lane of 4–12% gradient gels (Invitrogen). Blots were incubated with emerin antibody (1:1000) or alpha-tubulin antibody (1:5000) followed by IR Dye-conjugated secondary antibodies (1:5000) for multiplexed detection on the Odyssey imaging system.

Microscopy and image analysis

Cells were grown in Ibidi culture chambers, treated as indicated, and fixed in 4% PFA for 5 min, then permeabilized in IF buffer (PBS, 0.1% Tx100, 0.02% SDS, 10 mg/ml BSA) before staining with Hoechst DNA dye. Wells were rinsed in PBS before imaging on a Zeiss LSM 710 scanning confocal microscope with a 63 \times 1.4 NA objective. Images shown are single confocal slices. All image quantification was performed on maximum intensity projections of z-series with ImageJ. To quantify NE-localized protein levels, the DNA stain was used as a mask, and all GFP fluorescence within that mask was quantified.

For lysosomal staining, cells were prepared as described (Castellano *et al.*, 2017) with the following modifications. Following fixation in 4% PFA for 5 min, cells were rinsed in PBS, then permeabilized in freshly prepared 0.1% digitonin in PBS for 10 min at 4C. Cells were rinsed again in PBS, then blocked in 2% goat serum in PBS for 30 min before staining with LAMP1 antibody (1:100 in 2% goat serum) for 1–2 hr at RT. Cells were rinsed again in PBS, then stained with Alexa Fluor-conjugated secondary antibody and Hoechst DNA stain for 1 hr at RT.

Additional information

Funding

Funder	Grant reference number	Author
NIH Office of the Director	NS096786	Martin Hetzer
National Institute of General Medical Sciences	R01GM126829	Martin Hetzer
National Cancer Institute	P30 014195	Martin Hetzer
Chapman Foundation		Martin Hetzer
Helmsley Charitable Trust		Martin Hetzer

The funders had no role in study design, data collection and interpretation, or the decision to submit the work for publication.

Author contributions

Abigail Buchwalter, Conceptualization, Data curation, Formal analysis, Validation, Investigation, Visualization, Methodology, Writing—original draft, Project administration, Writing—review and editing; Roberta Schulte, Data curation, Investigation, Methodology, Project administration; Hsiao Tsai, Investigation, Methodology; Juliana Capitanio, Software, Formal analysis, Methodology; Martin Hetzer, Resources, Supervision, Funding acquisition, Writing—review and editing

Author ORCIDs

Abigail Buchwalter  <https://orcid.org/0000-0001-7181-6961>

Decision letter and Author response

Decision letter <https://doi.org/10.7554/eLife.49796.030>

Author response <https://doi.org/10.7554/eLife.49796.031>

Additional files

Supplementary files

- Source data 1. Filtered peptide data for half life calculations. Peptide turnover data for all peptides passing quality control filters. See R script and Materials and methods for details.

DOI: <https://doi.org/10.7554/eLife.49796.021>

- Source data 2. Filtered protein data for half life calculations. Filtered and averaged protein turnover data. See R script and Materials and methods for details.

DOI: <https://doi.org/10.7554/eLife.49796.022>

- Supplementary file 1. Results of half life fits passing quality filters.

DOI: <https://doi.org/10.7554/eLife.49796.023>

- Supplementary file 2. Complete list of half life fits.

DOI: <https://doi.org/10.7554/eLife.49796.024>

- Supplementary file 3. Half lives and protein topology data. Selected data related to **Figure 1G-H**.

DOI: <https://doi.org/10.7554/eLife.49796.025>

- Transparent reporting form DOI: <https://doi.org/10.7554/eLife.49796.026>

Data availability

Raw and analyzed mass spectrometric data and associated scripts and tables have been deposited in Dryad. Analyzed data are also included with the manuscript as supplementary tables.

The following dataset was generated:

Author(s)	Year	Dataset title	Dataset URL	Database and Identifier
Buchwalter A,	2019	Data from: Selective clearance of	https://dx.doi.org/10.7554/eLife.49796	Dryad Digital

Schulte R, Tsai H,
Capitanio J, Hetzer
MW

the inner nuclear membrane
protein emerin by vesicular
transport during ER stress

5061/dryad.n0r525h

Repository, 10.5061/
dryad.n0r525h

References

- Albert S**, Schaffer M, Beck F, Mosalaganti S, Asano S, Thomas HF, Plitzko JM, Beck M, Baumeister W, Engel BD. 2017. Proteasomes tether to two distinct sites at the nuclear pore complex. *PNAS* **114**:13726–13731. DOI: <https://doi.org/10.1073/pnas.1716305114>, PMID: 29229809
- Barlowe CK**, Miller EA. 2013. Secretory protein biogenesis and traffic in the early secretory pathway. *Genetics* **193**:383–410. DOI: <https://doi.org/10.1534/genetics.112.142810>
- Boni A**, Politi AZ, Strnad P, Xiang W, Hossain MJ, Ellenberg J. 2015. Live imaging and modeling of inner nuclear membrane targeting reveals its molecular requirements in mammalian cells. *The Journal of Cell Biology* **209**:705–720. DOI: <https://doi.org/10.1083/jcb.201409133>, PMID: 26056140
- Bonne G**, Quijano-Roy S. 2013. Emery-Dreifuss muscular dystrophy, Laminopathies, and other nuclear envelopathies. *Pediatric Neurology*:1367–1376. DOI: <https://doi.org/10.1016/B978-0-444-59565-2.00007-1>
- Brachner A**, Foisner R. 2011. Evolution of LEM proteins as chromatin tethers at the nuclear periphery. *Biochemical Society Transactions* **39**:1735–1741. DOI: <https://doi.org/10.1042/BST20110724>, PMID: 22103517
- Buchwalter A**, Hetzer MW. 2017. Nucleolar expansion and elevated protein translation in premature aging. *Nature Communications* **8**:328. DOI: <https://doi.org/10.1038/s41467-017-00322-z>, PMID: 28855503
- Bulbarelli A**, Sprocati T, Barberi M, Pedrazzini E, Borgese N. 2002. Trafficking of tail-anchored proteins: transport from the endoplasmic reticulum to the plasma membrane and sorting between surface domains in polarised epithelial cells. *Journal of Cell Science* **115**:1689–1702. PMID: 11950887
- Cambridge SB**, Gnad F, Nguyen C, Bermejo JL, Krüger M, Mann M. 2011. Systems-wide proteomic analysis in mammalian cells reveals conserved, functional protein turnover. *Journal of Proteome Research* **10**:5275–5284. DOI: <https://doi.org/10.1021/pr101183k>, PMID: 22050367
- Campeau E**, Ruhl VE, Rodier F, Smith CL, Rahmberg BL, Fuss JO, Campisi J, Yaswen P, Cooper PK, Kaufman PD. 2009. A versatile viral system for expression and depletion of proteins in mammalian cells. *PLOS ONE* **4**:e6529. DOI: <https://doi.org/10.1371/journal.pone.0006529>, PMID: 19657394
- Castellano BM**, Thelen AM, Moldavski O, Feltes M, van der Welle RE, Mydock-McGrane L, Jiang X, van Eijkeren RJ, Davis OB, Louie SM, Perera RM, Covey DF, Nomura DK, Ory DS, Zoncu R. 2017. Lysosomal cholesterol activates mTORC1 via an SLC38A9-Niemann-Pick C1 signaling complex. *Science* **355**:1306–1311. DOI: <https://doi.org/10.1126/science.aag1417>, PMID: 28336668
- Chardin P**, McCormick F. 1999. Brefeldin A: the advantage of being uncompetitive. *Cell* **97**:153–155. DOI: [https://doi.org/10.1016/S0092-8674\(00\)80724-2](https://doi.org/10.1016/S0092-8674(00)80724-2), PMID: 10219235
- Christianson JC**, Olzmann JA, Shaler TA, Sowa ME, Bennett EJ, Richter CM, Tyler RE, Greenblatt EJ, Harper JW. 2011. Defining human ERAD networks through an integrative mapping strategy. *Nature Publishing Group* **14**:93–105. DOI: <https://doi.org/10.1038/ncb2383>
- D'Angelo MA**, Raices M, Panowski SH, Hetzer MW. 2009. Age-dependent deterioration of nuclear pore complexes causes a loss of nuclear integrity in postmitotic cells. *Cell* **136**:284–295. DOI: <https://doi.org/10.1016/j.cell.2008.11.037>, PMID: 19167330
- Deldicque L**, Hespel P, Francaux M. 2012. Endoplasmic reticulum stress in skeletal muscle: origin and metabolic consequences. *Exercise and Sport Sciences Reviews* **40**:43–49. DOI: <https://doi.org/10.1097/JES.0b013e3182355e8c>, PMID: 21918459
- Demmerle J**, Koch AJ, Holaska JM. 2013. Emerin and histone deacetylase 3 (HDAC3) cooperatively regulate expression and nuclear positions of MyoD, Myf5, and Pax7 genes during myogenesis. *Chromosome Research* **21**:765–779. DOI: <https://doi.org/10.1007/s10577-013-9381-9>, PMID: 24062260
- Deshais RJ**, Joazeiro CA. 2009. RING domain E3 ubiquitin ligases. *Annual Review of Biochemistry* **78**:399–434. DOI: <https://doi.org/10.1146/annurev.biochem.78.101807.093809>, PMID: 19489725
- Dörrbaum AR**, Kochen L, Langer JD, Schuman EM. 2018. Local and global influences on protein turnover in neurons and Glia. *eLife* **7**:489. DOI: <https://doi.org/10.7554/eLife.34202>
- Fagioli C**, Sitia R. 2001. Glycoprotein quality control in the endoplasmic reticulum. *Journal of Biological Chemistry* **276**:12885–12892. DOI: <https://doi.org/10.1074/jbc.M009603200>
- Fairley EA**, Kendrick-Jones J, Ellis JA. 1999. The Emery-Dreifuss muscular dystrophy phenotype arises from aberrant targeting and binding of emerin at the inner nuclear membrane. *Journal of Cell Science* **112** (Pt 15):2571–2582. PMID: 10393813
- Farkas T**, Daugaard M, Jäättelä M. 2011. Identification of small molecule inhibitors of phosphatidylinositol 3-kinase and autophagy. *Journal of Biological Chemistry* **286**:38904–38912. DOI: <https://doi.org/10.1074/jbc.M111.269134>, PMID: 21930714
- Fellmann C**, Hoffmann T, Sridhar V, Hopfgartner B, Muhar M, Roth M, Lai DY, Barbosa IA, Kwon JS, Guan Y, Sinha N, Zuber J. 2013. An optimized microRNA backbone for effective single-copy RNAi. *Cell Reports* **5**:1704–1713. DOI: <https://doi.org/10.1016/j.celrep.2013.11.020>, PMID: 24332856
- Foresti O**, Ruggiano A, Hannibal-Bach HK, Ejnsing CS, Carvalho P. 2013. Sterol homeostasis requires regulated degradation of squalene monooxygenase by the ubiquitin ligase Doa10/Teb4. *eLife* **2**:e00953. DOI: <https://doi.org/10.7554/eLife.00953>, PMID: 23898401

- Gao R**, Schellenberg MJ, Huang SY, Abdelmalak M, Marchand C, Nitiss KC, Nitiss JL, Williams RS, Pommier Y. 2014. Proteolytic degradation of topoisomerase II (Top2) enables the processing of Top2-DNA and Top2-RNA covalent complexes by tyrosyl-DNA-phosphodiesterase 2 (TDP2). *Journal of Biological Chemistry* **289**:17960–17969. DOI: <https://doi.org/10.1074/jbc.M114.565374>, PMID: 24808172
- Guilluy C**, Osborne LD, Van Landeghem L, Sharek L, Superfine R, Garcia-Mata R, Burridge K. 2014. Isolated nuclei adapt to force and reveal a mechanotransduction pathway in the nucleus. *Nature Cell Biology* **16**:376–381. DOI: <https://doi.org/10.1038/ncb2927>, PMID: 24609268
- Harding HP**, Zhang Y, Ron D. 1999. Protein translation and folding are coupled by an endoplasmic-reticulum-resident kinase. *Nature* **397**:271–274. DOI: <https://doi.org/10.1038/16729>, PMID: 9930704
- He L**, Diedrich J, Chu YY, Yates JR. 2015. Extracting accurate precursor information for tandem mass spectra by RawConverter. *Analytical Chemistry* **87**:11361–11367. DOI: <https://doi.org/10.1021/acs.analchem.5b02721>, PMID: 26499134
- Heckman KL**, Pease LR. 2007. Gene splicing and mutagenesis by PCR-driven overlap extension. *Nature Protocols* **2**:924–932. DOI: <https://doi.org/10.1038/nprot.2007.132>, PMID: 17446874
- Hegde RS**, Zavodszky E. 2019. Recognition and Degradation of Mislocalized Proteins in Health and Disease. *Cold Spring Harbor Perspectives in Biology*. **19**:a033902. DOI: <https://doi.org/10.1101/cshperspect.a033902>
- Hofemeister H**, O'Hare P. 2005. Analysis of the localization and topology of nurim, a polytopic protein tightly associated with the inner nuclear membrane. *Journal of Biological Chemistry* **280**:2512–2521. DOI: <https://doi.org/10.1074/jbc.M410504200>
- Katta SS**, Smoyer CJ, Jaspersen SL. 2014. Destination: inner nuclear membrane. *Trends in Cell Biology* **24**:221–229. DOI: <https://doi.org/10.1016/j.tcb.2013.10.006>, PMID: 24268652
- Khmelniskii A**, Blaszcak E, Pantazopoulou M, Fischer B, Omnus DJ, Le Dez G, Brossard A, Gunnarsson A, Barry JD, Meurer M, Kirrmaier D, Boone C, Huber W, Rabut G, Ljungdahl PO, Knop M. 2014. Protein quality control at the inner nuclear membrane. *Nature* **516**:410–413. DOI: <https://doi.org/10.1038/nature14096>, PMID: 25519137
- Klionsky DJ**, Abdelmohsen K, Abe A, Abedin MJ, Abeliovich H, Acevedo Arozena A, Adachi H, Adams CM, Adams PD, Adeli K, Adhietty PJ, Adler SG, Agam G, Agarwal R, Aghi MK, Agnello M, Agostinis P, Aguilar PV, Aguirre-Ghiso J, Airoidi EM, et al. 2016. Guidelines for the use and interpretation of assays for monitoring autophagy (3rd edition). *Autophagy* **12**:1–222. DOI: <https://doi.org/10.1080/15548627.2015.1100356>
- Knott SRV**, Maceli A, Erard N, Chang K, Marran K, Zhou X, Gordon A, Demerdash OE, Wagenblast E, Kim S, Fellmann C, Hannon GJ. 2014. A computational algorithm to predict shRNA potency. *Molecular Cell* **56**:796–807. DOI: <https://doi.org/10.1016/j.molcel.2014.10.025>, PMID: 25435137
- Krogh A**, Larsson B, von Heijne G, Sonnhammer EL. 2001. Predicting transmembrane protein topology with a hidden markov model: application to complete genomes. *Journal of Molecular Biology* **305**:567–580. DOI: <https://doi.org/10.1006/jmbi.2000.4315>, PMID: 11152613
- Lee KK**, Haraguchi T, Lee RS, Koujin T, Hiraoka Y, Wilson KL. 2001. Distinct functional domains in Emerin Bind Lamin A and DNA-bridging protein BAF. *Journal of Cell Science* **114**:4567–4573. PMID: 11792821
- Leto DE**, Morgens DW, Zhang L, Walczak CP, Elias JE, Bassik MC, Kopito RR. 2019. Genome-wide CRISPR analysis identifies Substrate-Specific conjugation modules in ER-Associated degradation. *Molecular Cell* **73**:377–389. DOI: <https://doi.org/10.1016/j.molcel.2018.11.015>, PMID: 30581143
- Ong SE**, Mann M. 2006. A practical recipe for stable isotope labeling by amino acids in cell culture (SILAC). *Nature Protocols* **1**:2650–2660. DOI: <https://doi.org/10.1038/nprot.2006.427>, PMID: 17406521
- Park SK**, Aslanian A, McClatchy DB, Han X, Shah H, Singh M, Rauniyar N, Moresco JJ, Pinto AF, Diedrich JK, Delahunty C, Yates JR. 2014. Census 2: isobaric labeling data analysis. *Bioinformatics* **30**:2208–2209. DOI: <https://doi.org/10.1093/bioinformatics/btu151>, PMID: 24681903
- Pryszcz LP**, Huerta-Cepas J, Gabaldón T. 2011. MetaPhOrs: orthology and paralogy predictions from multiple phylogenetic evidence using a consistency-based confidence score. *Nucleic Acids Research* **39**:e32–. DOI: <https://doi.org/10.1093/nar/gkq953>, PMID: 21149260
- Rolls MM**, Stein PA, Taylor SS, Ha E, McKeon F, Rapoport TA. 1999. A visual screen of a Gfp-Fusion library identifies a new type of nuclear envelope membrane protein. *The Journal of Cell Biology* **146**:29–44. DOI: <https://doi.org/10.1083/jcb.146.1.29>
- Ruggiano A**, Foresti O, Carvalho P. 2014. Quality control: er-associated degradation: protein quality control and beyond. *The Journal of Cell Biology* **204**:869–879. DOI: <https://doi.org/10.1083/jcb.201312042>, PMID: 24637321
- Saftig P**, Klumperman J. 2009. Lysosome biogenesis and lysosomal membrane proteins: trafficking meets function. *Nature Reviews Molecular Cell Biology* **10**:623–635. DOI: <https://doi.org/10.1038/nrm2745>
- Satpute-Krishnan P**, Ajinkya M, Bhat S, Itakura E, Hegde RS, Lippincott-Schwartz J. 2014. ER stress-induced clearance of misfolded GPI-anchored proteins via the secretory pathway. *Cell* **158**:522–533. DOI: <https://doi.org/10.1016/j.cell.2014.06.026>, PMID: 25083867
- Schirmer EC**, Florens L, Guan T, Yates JR, Gerace L. 2003. Nuclear membrane proteins with potential disease links found by subtractive proteomics. *Science* **301**:1380–1382. DOI: <https://doi.org/10.1126/science.1088176>, PMID: 12958361
- Schreiber KH**, Kennedy BK. 2013. When lamins go bad: nuclear structure and disease. *Cell* **152**:1365–1375. DOI: <https://doi.org/10.1016/j.cell.2013.02.015>, PMID: 23498943
- Shimi T**, Koujin T, Segura-Totten M, Wilson KL, Haraguchi T, Hiraoka Y. 2004. Dynamic interaction between BAF and emerin revealed by FRAP, FLIP, and FRET analyses in living HeLa cells. *Journal of Structural Biology* **147**:31–41. DOI: <https://doi.org/10.1016/j.jsb.2003.11.013>, PMID: 15109603

- Smith MD**, Harley ME, Kemp AJ, Wills J, Lee M, Arends M, von Kriegsheim A, Behrends C, Wilkinson S. 2018. CCPG1 is a Non-canonical autophagy cargo receptor essential for ER-Phagy and pancreatic ER proteostasis. *Developmental Cell* **44**:217–232. DOI: <https://doi.org/10.1016/j.devcel.2017.11.024>, PMID: 29290589
- Tabb DL**, McDonald WH, Yates JR. 2002. DTASelect and contrast: tools for assembling and comparing protein identifications from shotgun proteomics. *Journal of Proteome Research* **1**:21–26. DOI: <https://doi.org/10.1021/pr015504q>, PMID: 12643522
- Toyama BH**, Savas JN, Park SK, Harris MS, Ingolia NT, Yates JR, Hetzer MW. 2013. Identification of long-lived proteins reveals exceptional stability of essential cellular structures. *Cell* **154**:971–982. DOI: <https://doi.org/10.1016/j.cell.2013.07.037>, PMID: 23993091
- Toyama BH**, Arrojo E, Drigo R, Lev-Ram V, Ramachandra R, Deerinck TJ, Lechene C, Ellisman MH, Hetzer MW. 2019. Visualization of long-lived proteins reveals age mosaicism within nuclei of postmitotic cells. *The Journal of Cell Biology* **218**:433–444. DOI: <https://doi.org/10.1083/jcb.201809123>, PMID: 30552100
- Tsai P-L**, Zhao C, Turner E, Schlieker C. 2016. The Lamin B receptor is essential for cholesterol synthesis and perturbed by disease-causing mutations. *eLife* **5**:4181. DOI: <https://doi.org/10.7554/eLife.16011>
- Uhlen M**, Fagerberg L, Hallstrom BM, Lindskog C, Oksvold P, Mardinoglu A, Sivertsson A, Kampf C, Sjostedt E, Asplund A, Olsson I, Edlund K, Lundberg E, Navani S, Szgyarto CA-K, Odeberg J, Djureinovic D, Takanen JO, Hober S, Alm T, et al. 2015. Tissue-based map of the human proteome. *Science* **347**:1260419–. DOI: <https://doi.org/10.1126/science.1260419>
- Ungricht R**, Klann M, Horvath P, Kutay U. 2015. Diffusion and retention are major determinants of protein targeting to the inner nuclear membrane. *The Journal of Cell Biology* **209**:687–704. DOI: <https://doi.org/10.1083/jcb.201409127>, PMID: 26056139
- Vaughan A**, Alvarez-Reyes M, Bridger JM, Broers JL, Ramaekers FC, Wehnert M, Morris GE, Whitfield WGF, Hutchison CJ. 2001. Both emerin and lamin C depend on lamin A for localization at the nuclear envelope. *Journal of Cell Science* **114**:2577–2590. PMID: 11683386
- Verzijlbergen KF**, Menendez-Benito V, van Welsem T, van Deventer SJ, Lindstrom DL, Ovaa H, Neefjes J, Gottschling DE, van Leeuwen F. 2010. Recombination-induced tag exchange to track old and new proteins. *PNAS* **107**:64–68. DOI: <https://doi.org/10.1073/pnas.0911164107>, PMID: 20018668
- Wang Q**, Li L, Ye Y. 2008. Inhibition of p97-dependent protein degradation by eeyarestatin I. *Journal of Biological Chemistry* **283**:7445–7454. DOI: <https://doi.org/10.1074/jbc.M708347200>, PMID: 18199748
- Xu T**, Park SK, Venable JD, Wohlschlegel JA, Diedrich JK, Cociorva D, Lu B, Liao L, Hewel J, Han X, Wong CCL, Fonslow B, Delahunty C, Gao Y, Shah H, Yates JR. 2015. ProLuCID: an improved SEQUEST-like algorithm with enhanced sensitivity and specificity. *Journal of Proteomics* **129**:16–24. DOI: <https://doi.org/10.1016/j.jprot.2015.07.001>, PMID: 26171723
- Zattas D**, Berk JM, Kreft SG, Hochstrasser M. 2016. A conserved C-terminal element in the yeast Doa10 and human MARCH6 ubiquitin ligases required for selective substrate degradation. *Journal of Biological Chemistry* **291**:12105–12118. DOI: <https://doi.org/10.1074/jbc.M116.726877>, PMID: 27068744
- Zavodszky E**, Hegde RS. 2019. Misfolded GPI-anchored proteins are escorted through the secretory pathway by ER-derived factors. *eLife* **8**:32. DOI: <https://doi.org/10.7554/eLife.46740>
- Zhang K**, Sha J, Harter ML. 2010. Activation of Cdc6 by MyoD is associated with the expansion of quiescent myogenic satellite cells. *The Journal of Cell Biology* **188**:39–48. DOI: <https://doi.org/10.1083/jcb.200904144>, PMID: 20048262